

Rotation-Invariant Transformer for Point Cloud Matching

Hao Yu¹ Zheng Qin² Ji Hou³ Mahdi Saleh¹ Dongsheng Li² Benjamin Busam¹ Slobodan Ilic^{1,4}

¹TUM ²NUDT ³Meta Reality Labs ⁴Siemens AG, Munich

Abstract

The intrinsic rotation invariance lies at the core of matching point clouds with handcrafted descriptors, but it is despised by most of the recent deep matchers. As an alternative, they obtain the rotation invariance extrinsically via data augmentation. However, the continuous $SO(3)$ space can never be covered by the finite number of augmented rotations, resulting in their instability when facing rotations that are rarely seen. To this end, we introduce RoITr, a **Rotation-Invariant Transformer** to cope with the pose variations in the point cloud matching task. We contribute both on the local and global levels. Starting from the local level, we introduce an attention mechanism embedded with Point Pair Feature (PPF)-based coordinates to describe the pose-invariant geometry, upon which a novel attention-based encoder-decoder is constructed. We further propose a global transformer with rotation-invariant cross-frame spatial awareness learned by the self-attention mechanism, which significantly improves the feature distinctiveness and makes the model robust with respect to the low overlap. Experiments are conducted on both the rigid and non-rigid public benchmarks, where RoITr outperforms all the state-of-the-art models by a considerable margin in the low-overlapping scenarios. Especially when the rotations are enlarged on the challenging 3DLoMatch benchmark, RoITr surpasses the existing methods by at least 13 and 5 percentage points in terms of Inlier Ratio and Registration Recall, respectively. Code will be made publicly available.

1. Introduction

The correspondence estimation between a pair of partially-overlapping point clouds is a long-standing task that lies at the core of many computer vision applications, such as tracking [17, 18], reconstruction [23, 24], pose estimation [19, 29, 50] and 3D representation learning [15, 16, 46], etc. In a typical solution, geometry is first encoded into descriptors, and correspondences are then established between two frames by matching the closest descriptors in the feature space. As the two frames are ob-

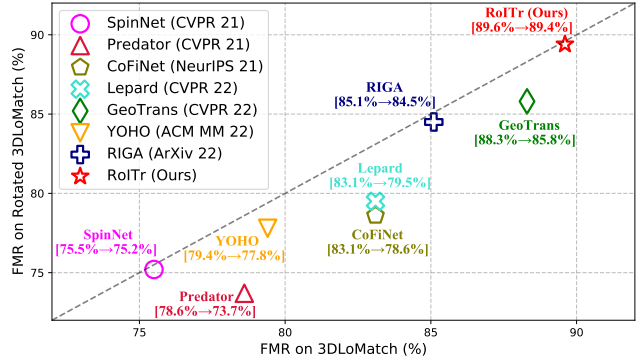


Figure 1. Feature Matching Recall (FMR) on 3DLoMatch [19] and Rotated 3DLoMatch. Distance to the diagonal represents the robustness against rotations. Among all the state-of-the-art approaches, RoITr not only ranks first on both benchmarks, but also shows the best robustness against the enlarged rotations.

served from different views, depicting the same geometry under different transformations identically, *i.e.*, the pose-invariance, becomes the key to success in the point cloud matching task.

Since the side effects caused by a global translation can always be easily eliminated, *e.g.*, by aligning the barycenter with the origin, the attention naturally shifts to coping with the rotations. In the past, handcrafted local descriptors [11, 31, 32, 41] were designed to be rotation-invariant so that the same geometry observed from different views can be correctly matched. With the emergence of deep neural models for 3D point analysis, *e.g.*, multilayer perceptrons (MLPs)-based like PointNet [27, 28], convolutions-based like KPConv [6, 40], and the attention-based like PointTransformer [34, 54], recent approaches [1, 7, 9, 10, 13, 19, 21, 29, 33, 48–50, 52] propose to learn descriptors from raw points as an alternative to handcrafted features that are less robust to occlusion and noise. The majority of deep point matchers [7, 10, 19, 21, 29, 35, 48, 50, 52, 53] is sensitive to rotations. Consequently, their invariance to rotations must be obtained extrinsically via augmented training to ensure that the same geometry under different poses can be depicted similarly. However, as the training cases can never span the continuous $SO(3)$ space, they always suffer from instability when facing rotations that are not covered by the

training. This can be seen by a significant performance drop under enlarged rotations at inference time. (See Fig. 1.)

There are other works [1, 9, 13, 33, 44] that only leverage deep neural networks to encode the pure geometry with the intrinsically designed rotation invariance. However, the intrinsic rotation invariance comes at the cost of losing global context. For example, a human’s left and right half are identically described, which naturally degrades the distinctiveness of features. Most recently, RIGA [49] is proposed to enhance the distinctiveness of the intrinsically rotation-invariant descriptors by incorporating a global context, *i.e.*, the left and right half of a human become distinguishable by knowing there is a chair on the left while a table on the right. However, it lacks a highly-representative rotation-invariant geometry encoder since it relies on the PointNet [27], which accounts for an ineffective local geometry description. Moreover, as depicting the cross-frame spatial positions is non-trivial, previous works [19, 29, 35, 50] merely leverage the contextual features in cross-attention, which totally neglects the spatial relationships. Although RIGA obtains the cross-frame spatial awareness in a rotation-invariant fashion, its awareness from a simple PointNet is still insufficient for learning distinctive descriptors.

In this paper, we present **Rotation-Invariant Transformer** (RoITr) to tackle the problem of point cloud matching under arbitrary pose variations. By leveraging Point Pair Features (PPFs) as the local coordinate representation, we first propose a local attention mechanism to learn the pure local geometry regardless of the varying poses. Upon it, attention-based layers are further proposed to compose the encoder-decoder architecture for highly-discriminative and rotation-invariant geometry encoding. We demonstrate its superiority over PointTransformer [54], a state-of-the-art attention-based backbone network, in terms of both efficiency and efficacy in Fig. 7 and Tab. 4 (a), respectively. On the global level, cross-frame awareness of spatial positions is introduced by the self-attention mechanism in a rotation-invariant fashion to facilitate feature distinctiveness. We illustrate its significance over the state-of-the-art design [29] in Tab. 4 (d). Our main contributions are summarized as:

- A local attention mechanism designed to disentangle the geometry and poses, which enables the pose-agnostic geometry description.
- An attention-based encoder-decoder architecture that learns highly-discriminative local geometry in a rotation-invariant fashion.
- A global transformer with rotation-invariant cross-frame position awareness that significantly enhances the feature distinctiveness.

2. Related Work

Methods with Extrinsic Rotation Invariance. The mainstream of deep learning-based point cloud matching ap-

proaches is intrinsically rotation-sensitive. Pioneers [10, 52] learn to describe local patches from a rotation-variant input. FCGF [7] leverages fully-convolutional networks to accelerate geometry description. D3Feat [3] jointly detects and describes sparse keypoints for matching. Predator [19] incorporates the global context to enhance the local descriptors and predicts the overlap regions for point sampling. CoFiNet [50] extracts coarse-to-fine correspondences to alleviate the repeatability issue of keypoints. GeoTrans [29] considers the geometric information in fusing the intra-frame information globally. However, the awareness of spatial positions is missing in their cross-frame fusion. Leopard [21] extends the non-rigid shape matching [35, 42] to point clouds and proposes a re-positioning module to alleviate the pose variations. REGTR [48] directly regresses the corresponding coordinates and registers point clouds in an end-to-end fashion. However, all of these methods suffer from instability with additional rotations.

Models with Intrinsic Rotation Invariance. A branch of handcrafted descriptors [8, 14, 41] align the input to a canonical representation according to an estimated local reference frame (LRF), while the others [11, 31, 32] mine the rotation-invariant components and encode them as the representation of the local geometry. Inspired by that, some deep learning-based methods [1, 4, 9, 13, 33, 35, 49] are designed to be intrinsically rotation-invariant to make the neural models focus on the pose-agnostic pure geometry. As a pioneer, PPF-FoldNet [9] consumes PPF-based patches and learns the descriptors using a FoldingNet [47]-based architecture without supervision. LRF-based works [1, 13, 33, 35] achieve rotation invariance by aligning their input to the defined canonical representation. YOHO [44] adopts a group of rotations to learn a rotation-equivariant feature group and further obtain the invariance via group pooling. A common problem of the rotation-invariant methods is the less distinctive features. To address the issue, RIGA [49] incorporates the global context into local descriptors, which significantly enhances the feature distinctiveness. However, the ineffective local geometry encoding and global position description restrict its performance.

3. Method

An overview of RoITr can be found in Fig. 2. RoITr consists of an encoder-decoder architecture named Point Pair Feature Transformer (PPFTrans) for geometry encoding and a stack of $g \times$ global transformers for global context aggregation. The correspondences \mathcal{C} are extracted by matching features in a coarse-to-fine manner [50].

3.1. Problem Statement

We tackle the problem of matching a pair of partially-overlapping point clouds $\mathbf{P} \in \mathbb{R}^{n \times 3}$ and $\mathbf{Q} \in \mathbb{R}^{m \times 3}$. We aim at extracting a correspondence set $\mathcal{C} = \{(\mathbf{p}_i, \mathbf{q}_j) | \mathbf{p}_i \in$

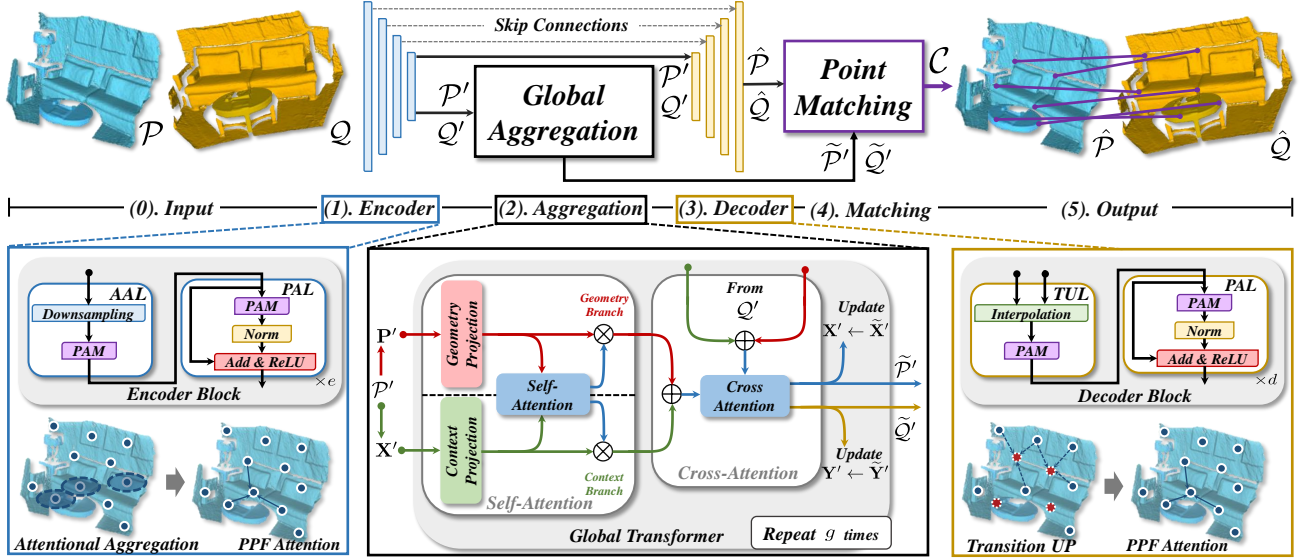


Figure 2. **An Overview of RoITr.** From left to right: **(0).** RoITr takes as input a pair of triplets $\mathcal{P} = (\mathbf{P}, \mathbf{N}, \mathbf{X})$ and $\mathcal{Q} = (\mathbf{Q}, \mathbf{M}, \mathbf{Y})$, both with three dimensions referring to the point cloud, the estimated normals, and the initial features. **(1)**[§. 3.2]. A stack of encoder blocks hierarchically downsamples the points to coarser superpoints and encodes the local geometry, yielding superpoint triplets \mathcal{P}' and \mathcal{Q}' . Each encoder block consists of an Attentional Abstraction Layer (AAL) for downsampling and abstraction, followed by $e \times$ PPF Attention Layers (PALs) for local geometry encoding and context aggregation. Both of them are based on our proposed PPF Attention Module (PAM), which enables the pose-agnostic encoding of pure geometry. (See Fig. 3). **(2)**[§. 3.3]. Global information is fused to enhance the superpoint features \mathbf{X}' and \mathbf{Y}' . Specially, the geometric cues are globally aggregated as a rotation-invariant position representation, which introduces spatial awareness in the coupled cross-frame context aggregation. After a stack of $g \times$ global transformers, the globally-enhanced triplets $\hat{\mathcal{P}}'$ and $\hat{\mathcal{Q}}'$ are produced. **(3)**[§. 3.2] Superpoint triplets \mathcal{P}' and \mathcal{Q}' are decoded to point triplets $\hat{\mathcal{P}}$ and $\hat{\mathcal{Q}}$ by a stack of decoder blocks. Each block consists of a Transition Up Layer (TUL) for upsampling and context aggregation, followed by $d \times$ PALs built upon PAM. **(4)**[§. 3.4] Correspondence set \mathcal{C} is generated in a coarse to fine manner [50] by matching $\hat{\mathcal{P}}'$ and $\hat{\mathcal{Q}}'$ first and matching $\hat{\mathcal{P}}$ and $\hat{\mathcal{Q}}$ consecutively. See the context for more details. **(5).** \mathcal{C} is finally established between $\hat{\mathcal{P}}$ and $\hat{\mathcal{Q}}$.

$\mathbf{P}, \mathbf{q}_j \in \mathcal{Q}$ minimizing:

$$\frac{1}{|\mathcal{C}|} \sum_{(\mathbf{p}_i, \mathbf{q}_j) \in \mathcal{C}} \|\mathcal{M}^*(\mathbf{p}_i) - \mathbf{q}_j\|_2, \quad (1)$$

where $\|\cdot\|_2$ denotes the Euclidean norm and $|\cdot|$ is the set cardinality. $\mathcal{M}^*(\cdot)$ stands for the ground-truth mapping function that maps \mathbf{p}_i to its corresponding position in \mathcal{Q} . In rigid scenarios, it is defined by a transformation $\mathbf{T} \in SE(3)$. For the non-rigid cases it can be denoted as a per-point flow $\mathbf{f}_i \in \mathbb{R}^3$ known as the deformation field.

3.2. PPFTrans for Geometry Description

Overview. Taking point cloud \mathbf{P} as an example, PPFTrans consumes a triplet $\mathcal{P} = (\mathbf{P}, \mathbf{N}, \mathbf{X})$, with $\mathbf{P} \in \mathbb{R}^{n \times 3}$ the points cloud, $\mathbf{N} \in \mathbb{R}^{n \times 3}$ the normals estimated from \mathbf{P} , and $\mathbf{X} = \vec{\mathbf{I}} \in \mathbb{R}^{n \times 1}$ the initial point features. The encoder produces the superpoint triplet $\mathcal{P}' = (\mathbf{P}', \mathbf{N}', \mathbf{X}')$, with n' superpoints and $\mathbf{X}' \in \mathbb{R}^{n' \times c'}$. With the consecutive decoder, \mathcal{P}' is decoded to a triplet $\hat{\mathcal{P}} = (\hat{\mathbf{P}}, \hat{\mathbf{N}}, \hat{\mathbf{X}})$ including \hat{n} points with features $\hat{\mathbf{X}} \in \mathbb{R}^{\hat{n} \times \hat{c}}$. Notably, as we adopt a Farthest Point Sampling (FPS) strategy [28], it always satisfies that $\mathbf{P}' \subseteq \hat{\mathbf{P}} \subseteq \mathbf{P}$ and $\mathbf{N}' \subseteq \hat{\mathbf{N}} \subseteq \mathbf{N}$. The same goes for a second point cloud \mathcal{Q} with an input

triplet $\mathcal{Q} = (\mathbf{Q} \in \mathbb{R}^{m \times 3}, \mathbf{M} \in \mathbb{R}^{m \times 3}, \mathbf{Y} = \vec{\mathbf{I}} \in \mathbb{R}^{m \times 1})$ by the shared architecture. In the rest of this paper, we only demonstrate for \mathcal{P} unless the model processes \mathcal{Q} differently. We further define the *Anchor* triplet as $\mathcal{P}^A = (\mathbf{P}^A, \mathbf{N}^A, \mathbf{X}^A)$ with n^A points and $\mathbf{X}^A \in \mathbb{R}^{n^A \times c^A}$, and the *Supporter* triplet $\mathcal{P}^S = (\mathbf{P}^S, \mathbf{N}^S, \mathbf{X}^S)$ with n^S points and $\mathbf{X}^S \in \mathbb{R}^{n^S \times c^S}$ for the following demonstration. It always holds that $\mathbf{P}^A \subseteq \mathbf{P}^S \subseteq \mathbf{P}$ and $\mathbf{N}^A \subseteq \mathbf{N}^S \subseteq \mathbf{N}$.

3.2.1 Pose-Agnostic Local Coordinates

The basis of PPFTrans is the pose-agnostic local coordinate representation that we construct based on PPFs. We detail the construction on *Supporter* triplet \mathcal{P}^S w.r.t. the *Anchor* triplet \mathcal{P}^A hereafter. Let $\mathcal{P}_i^A := (\mathbf{p}_i^A \in \mathbf{P}^A, \mathbf{n}_i^A \in \mathbf{N}^A, \mathbf{x}_i^A \in \mathbf{X}^A) \in \mathcal{P}^A$ denote the triplet constructed by picking the corresponding item on each dimension. For each \mathcal{P}_i^A , its k -nearest neighbors in \mathcal{P}^S are first retrieved according to the Euclidean distance between \mathbf{p}_i^A and \mathbf{P}^S , denoted as $\mathcal{P}_{\mathcal{N}(i)}^S := (\mathbf{P}_{\mathcal{N}(i)}^S, \mathbf{N}_{\mathcal{N}(i)}^S, \mathbf{X}_{\mathcal{N}(i)}^S) \subseteq \mathcal{P}^S$, with $\mathcal{N}(i)$ the k -nearest neighbors. We then adopt PPFs to construct a local coordinate system around each \mathbf{p}_i^A to represent the pose-agnostic position of $\mathbf{P}_{\mathcal{N}(i)}^S$ w.r.t. it. The coordi-

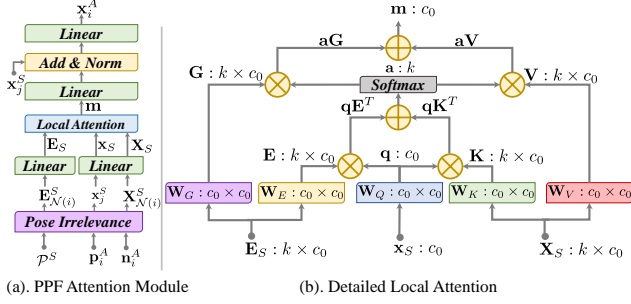


Figure 3. **Left:** The workflow of the PPF Attention Module (PAM). **Right:** The computation of the local attention.

nate of point $\mathbf{p}_j^S \in \mathbf{P}_{\mathcal{N}(i)}^S$ is transferred to:

$$\mathbf{e}_j^S = (\|\mathbf{d}\|_2, \angle(\mathbf{n}_i^A, \mathbf{d}), \angle(\mathbf{n}_j^S, \mathbf{d}), \angle(\mathbf{n}_j^S, \mathbf{n}_i^A)), \quad (2)$$

with $\mathbf{d} = \mathbf{p}_j^S - \mathbf{p}_i^A$, and \mathbf{n}_i^A and \mathbf{n}_j^S the estimated normals of \mathbf{p}_i^A and \mathbf{p}_j^S , respectively. $\angle(\mathbf{v}_1, \mathbf{v}_2)$ computes the angles between the two vectors [5, 9]. The transferred coordinates of $\mathbf{P}_{\mathcal{N}(i)}^S$ are denoted as $\mathbf{E}_{\mathcal{N}(i)}^S$.

3.2.2 PPF Attention Module

The core component of PPFTrans is the PPF Attention Module (PAM) that takes as input a *Supporter* triplet \mathcal{P}^S . With the *Anchor* point cloud \mathbf{P}^A and associated normals \mathbf{N}^A known, PAM generates the *Anchor* features \mathbf{X}^A by aggregating the pose-agnostic local geometry and highly-representative learned context from \mathcal{P}^S . PAM can be defined as:

$$\mathcal{P}^A = \delta(\mathbf{P}^A; \mathbf{N}^A | \mathcal{P}^S). \quad (3)$$

As shown in Fig. 3 (a), for each $\mathbf{p}_i^A \in \mathbf{P}^A$ with normal \mathbf{n}_i^A , we find its corresponding point $\mathbf{p}_j^S \in \mathbf{P}^S$ whose associated feature \mathbf{x}_j^S is assigned to \mathbf{p}_i^A as the initial description. Then, k -nearest neighbors from \mathbf{P}^S are retrieved according to the Euclidean distance in 3D space, yielding $\mathbf{P}_{\mathcal{N}(i)}^S \subseteq \mathbf{P}^S$ and $\mathbf{X}_{\mathcal{N}(i)}^S \subseteq \mathbf{X}^S$. Following Eq. 2, $\mathbf{P}_{\mathcal{N}(i)}^S$ is transferred to the pose-agnostic position representation $\mathbf{E}_{\mathcal{N}(i)}^S$ which is consecutively projected to the coordinate embedding \mathbf{E}_S via a linear layer. \mathbf{x}_j^S and $\mathbf{X}_{\mathcal{N}(i)}^S$ are projected to the contextual features \mathbf{x}_S and \mathbf{X}_S by a second shared linear layer, respectively. In Fig. 3 (b), the designed local attention mechanism uses five learnable matrices \mathbf{W}_G , \mathbf{W}_E , \mathbf{W}_Q , \mathbf{W}_K , and \mathbf{W}_V to further project the input features. Specifically, \mathbf{W}_G and \mathbf{W}_E project the input coordinate embedding to the geometric representation and positional encoding by:

$$\mathbf{G} = \mathbf{E}_S \mathbf{W}_G, \quad \mathbf{E} = \mathbf{E}_S \mathbf{W}_E, \quad (4)$$

respectively. Similarly, \mathbf{W}_Q , \mathbf{W}_K , and \mathbf{W}_V project the learned context to *Query*, *Key*, and *Value* as:

$$\mathbf{q} = \mathbf{x}_S \mathbf{W}_Q, \quad \mathbf{K} = \mathbf{X}_S \mathbf{W}_K, \quad \mathbf{V} = \mathbf{X}_S \mathbf{W}_V, \quad (5)$$

respectively, where \mathbf{q} and \mathbf{K} are used for retrieving similar context and \mathbf{V} encodes the contextual messages flowing from *Supporter* to *Anchor*. The attention vector \mathbf{a} that measures the contextual similarity between *Anchor* and *Supporter*, and the message \mathbf{m} that encodes both the pose-agnostic geometry and the representative context read as:

$$\mathbf{a} = \text{Softmax}\left(\frac{\mathbf{q}\mathbf{E}^T + \mathbf{q}\mathbf{K}^T}{\sqrt{c_0}}\right) \quad \text{and} \quad \mathbf{m} = \mathbf{a}\mathbf{G} + \mathbf{a}\mathbf{V}, \quad (6)$$

respectively. The message \mathbf{m} is further projected and aggregated to \mathbf{x}_j^S via an element-wise addition followed by a normalization through LayerNorm [2]. A final linear layer projects the obtained feature to $\mathbf{x}_i^A \in \mathbb{R}^{c_A}$, from which \mathbf{X}^A is finally obtained to formulate the output \mathcal{P}^A with the known \mathbf{P}^A and \mathbf{N}^A .

3.2.3 Encoder and Decoder Blocks

Encoder. We construct our encoder by stacking several encoder blocks, each consisting of an Attentional Abstraction Layer (AAL) followed by $e \times$ PPF Attention Layers (PALs). The encoder block takes as input the *Supporter* triplet \mathcal{P}^S which consecutively flows to AAL, where \mathbf{P}^S is down-sampled to obtain the *Anchor* points \mathbf{P}^A with associated normals \mathbf{N}^A via FPS [28]. The *Anchor* triplet \mathcal{P}^A is consecutively generated in AAL via a PAM as $\mathcal{P}^A = \delta(\mathbf{P}^A; \mathbf{N}^A | \mathcal{P}^S)$ according to Eq. 3. A sequence of $e \times$ PALs is applied for further enhancing the *Anchor* features \mathbf{X}^A , with each PAL updating the features as:

$$\mathcal{P}^A \leftarrow \theta(\mathcal{P}^A) = \text{ReLU}(\mathbf{X}^A + \phi(\delta(\mathbf{P}^A; \mathbf{N}^A | \mathcal{P}^A))), \quad (7)$$

with ϕ the LayerNorm [2] and δ the PAM of PAL. $\mathcal{P}^A \leftarrow \theta(\mathcal{P}^A)$ depicts updating the features of \mathcal{P}^A with the output of PAL. The output of the encoder is defined as $\mathcal{P}' := \mathcal{P}^A$, with \mathcal{P}^A the output of the last encoder block.

Decoder. We construct the decoder part by stacking a series of decoder blocks, including a Transition Up Layer (TUL) followed by $d \times$ PAL. The encoder block takes as input both the *Anchor* triplet \mathcal{P}^A and the *Supporter* triplet \mathcal{P}^S , where \mathcal{P}^S is from the encoder via skip connections. The input is forwarded to the Transition Up Layer (TUL), where each $\tilde{\mathbf{x}}_j^S \in \tilde{\mathbf{X}}^S$ is interpolated by:

$$\tilde{\mathbf{x}}_j^S = \frac{\sum_{i \in \mathcal{N}(j)} w_i^j \mathbf{x}_i^A}{\sum_{i \in \mathcal{N}(j)} w_i^j}, \quad \text{with } w_i^j = \frac{1}{\|\mathbf{p}_j^S - \mathbf{p}_i^A\|_2}, \quad (8)$$

with $\mathcal{N}(j)$ the k -nearest neighbors of \mathbf{p}_j^S . *Supporter* features are updated by two linear layers as $\mathcal{P}^S \leftarrow \zeta_1(\mathbf{X}^S) + \zeta_2(\tilde{\mathbf{X}}^S)$. A sequence of $d \times$ PALs are adopted after the TUL, with each enhancing the features as $\mathcal{P}^S \leftarrow \theta(\mathcal{P}^S)$ according to Eq. 7. The output of decoder is denoted as $\tilde{\mathcal{P}} := \mathcal{P}^S$, with \mathcal{P}^S the output of the last decoder block.

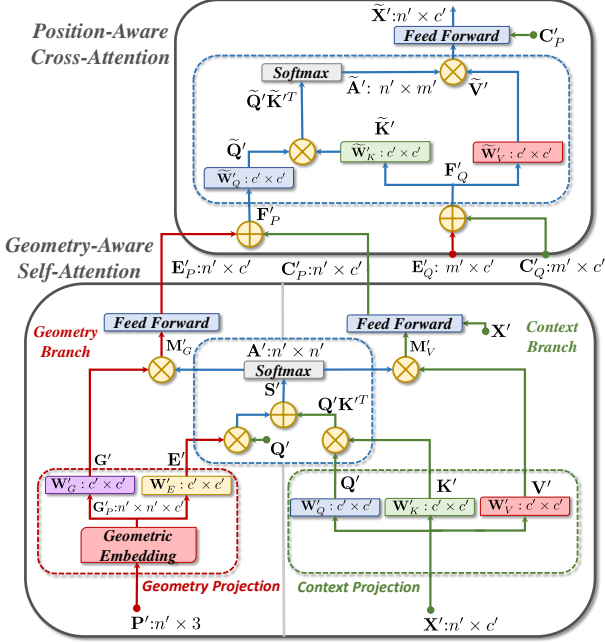


Figure 4. The computation graph of our global transformer consisting of the coupled Geometry-Aware Self-Attention Module (GSM) and Position-Aware Cross-Attention Module (PCM).

3.3. Global Transformer for Context Aggregation

Overview. Different from previous works [19, 29, 48–50] that disentangle the self- and cross-attention as individual modules, we couple them together as a global transformer, with the cross-frame spatial awareness learned by the self-attention in a rotation-invariant manner. The global transformer takes as input a pair of triplets \mathcal{P}' and \mathcal{Q}' , and enhances the features with the global context, yielding $\tilde{\mathbf{X}}' \in \mathbb{R}^{n' \times c'}$ and $\tilde{\mathbf{Y}}' \in \mathbb{R}^{m' \times c'}$, respectively. We stack $g \times$ global transformers, with each including a Geometry-Aware Self-Attention Module (GSM) and a Position-Aware Cross-Attention Module (PCM) (See Fig. 2 and Fig. 4).

Geometry-Aware Self-Attention Module. We detail GSM at the bottom of Fig. 4. GSM has two branches, where the geometry branch mines the geometric cues from the geometric embedding proposed in [29], and the context branch aggregates the global context across the frame. We refer the readers to the Appendix for the detailed construction of the pairwise geometric embedding $\mathbf{G}'_P \in \mathbb{R}^{n' \times n' \times c'}$. Similar to Eq. 4, the geometric context \mathbf{G}' and the positional encoding \mathbf{E}' are linearly projected from \mathbf{G}'_P by two learnable matrices in the geometry branch, respectively. \mathbf{E}' is further processed in the geometry branch and finally leveraged as the rotation-invariant cross-frame position awareness. In the context branch, \mathbf{Q}' , \mathbf{K}' , and \mathbf{V}' are obtained by linearly mapping the input features \mathbf{X}' with the corresponding matrices in a similar way as Eq. 5. Then the hybrid score matrix $\mathbf{S}' \in \mathbb{R}^{n' \times n'}$ is computed as the similarity from both

the geometric and contextual information:

$$\mathbf{S}'(i, j) = \frac{(\mathbf{q}'_i)(\mathbf{e}'_{i,j} + \mathbf{k}'_j)^T}{\sqrt{c'}}, \quad (9)$$

with $\mathbf{e}'_{i,j} := \mathbf{E}'(i, j, :)$, $\mathbf{q}'_i := \mathbf{Q}'(i, :)$, and $\mathbf{k}'_j := \mathbf{K}'(j, :)$ the c' -dimension vectors. The hybrid attention \mathbf{A}' is obtained via a Softmax function over each row of \mathbf{S}' , and the geometric messages $\mathbf{M}'_G \in \mathbb{R}^{n' \times c'}$ are computed as:

$$\mathbf{M}'_G(i, :) = \sum_{1 \leq j \leq n'} a'_{i,j} \mathbf{g}'_{i,j}, \quad (10)$$

with $a'_{i,j} := \mathbf{A}'(i, j)$ and $\mathbf{g}'_{i,j} := \mathbf{G}'(i, j, :)$. The contextual messages $\mathbf{M}'_V \in \mathbb{R}^{n' \times c'}$ are computed by $\mathbf{A}'\mathbf{V}'$. After a feed-forward network [43], global positional encoding \mathbf{E}'_P and globally-enhanced context \mathbf{C}'_P are generated.

Position-Aware Cross-Attention Module. The PCM consumes a pair of doublets $(\mathbf{E}'_P, \mathbf{C}'_P)$ and $(\mathbf{E}'_Q, \mathbf{C}'_Q)$ that are generated from \mathcal{P}' and \mathcal{Q}' by a shared GSM, respectively. As the cross-attention is directional, we apply the same PCM twice, with the first aggregation from \mathcal{Q}' to \mathcal{P}' (See the top part of Fig. 4), and the second reversed. As the first step, the rotation-invariant spatial representation is incorporated to make the consecutive cross-attention position-aware, yielding position-aware features $\mathbf{F}'_P = \mathbf{E}'_P + \mathbf{C}'_P \in \mathbb{R}^{n' \times c'}$ and $\mathbf{F}'_Q = \mathbf{E}'_Q + \mathbf{C}'_Q \in \mathbb{R}^{m' \times c'}$. Similar to Eq. 5, $\tilde{\mathbf{Q}}'$, $\tilde{\mathbf{K}}'$, and $\tilde{\mathbf{V}}'$ are defined as the linear projection of \mathbf{F}'_P , \mathbf{F}'_Q , and \mathbf{F}'_Q , respectively. The attention matrix $\tilde{\mathbf{A}} \in \mathbb{R}^{n' \times m'}$ is computed via a row-wise softmax function applied on $\tilde{\mathbf{Q}}' \tilde{\mathbf{K}}'^T$. The fused messages are presented as $\tilde{\mathbf{A}} \tilde{\mathbf{V}}'$, which are finally mapped to the output features $\tilde{\mathbf{X}}'$ through a feed-forward network. As we introduce spatial awareness at the beginning of PCM, both the attention computation and message fusion are aware of the cross-frame positions. After the twice application of PCM, the input features are enhanced as $\mathcal{P}' \leftarrow \tilde{\mathbf{X}}'$ and $\mathcal{Q}' \leftarrow \tilde{\mathbf{Y}}'$, respectively. The global aggregation stage finally generates a pair of triplets $\mathcal{P}' := (\mathbf{P}', \mathbf{N}', \tilde{\mathbf{X}}')$ and $\mathcal{Q}' := (\mathbf{Q}', \mathbf{M}', \tilde{\mathbf{Y}}')$, with the enhanced features from the last global transformer.

3.4. Point Matching and Loss Function

Superpoint Matching. As shown in Fig. 2, the point matching stage takes as input a pair of superpoint triplets $\tilde{\mathcal{P}}'$ and $\tilde{\mathcal{Q}}'$ output by the global aggregation stage, as well as a pair of point triplets $\hat{\mathcal{P}}$ and $\hat{\mathcal{Q}}$ produced by the decoder. We adopt the coarse-to-fine matching strategy proposed in [50] for feature-based point matching. Following [29], we first normalize the superpoint features $\tilde{\mathbf{X}}'$ and $\tilde{\mathbf{Y}}'$ on to a unit hypersphere, and measure the pairwise similarity using a Gaussian correlation matrix $\tilde{\mathbf{S}}$ with $\tilde{\mathbf{S}}(i, j) = -\exp(-\|\tilde{\mathbf{x}}'_i - \tilde{\mathbf{y}}'_j\|_2^2)$. After a dual-normalization [29, 30, 38] on $\tilde{\mathbf{S}}$ for global feature correlation, superpoints associated to

the top- k entries are selected as the coarse correspondence set $\mathcal{C}' = \{(\mathbf{p}'_i, \mathbf{q}'_j) | \mathbf{p}'_i \in \mathbf{P}', \mathbf{q}'_j \in \mathbf{Q}'\}$.

Point Matching. For extracting point correspondences from \mathcal{C}' , denser points $\hat{\mathbf{P}}$ and $\hat{\mathbf{Q}}$ are first assigned to superpoints. To this end, the point-to-node strategy [50] is leveraged, where each point is assigned to its closest superpoint in 3D space. Given a superpoint $\mathbf{p}'_i \in \mathbf{P}'$, the group of points assigned to it is denoted as $\hat{\mathbf{G}}_i^P$ with $\hat{\mathbf{G}}_i^P \subseteq \hat{\mathbf{P}}$. The group of features associated to $\hat{\mathbf{G}}_i^P$ is further defined as $\hat{\mathbf{G}}_i^X$ with $\hat{\mathbf{G}}_i^X \subseteq \hat{\mathbf{X}}$. For each superpoint correspondence $\mathcal{C}'_l = (\mathbf{p}'_i, \mathbf{q}'_j)$, the similarity between the corresponding feature groups $\hat{\mathbf{G}}_i^X$ and $\hat{\mathbf{G}}_j^Y$ is calculated as $\hat{\mathbf{S}}_l = \hat{\mathbf{G}}_i^X (\hat{\mathbf{G}}_j^Y)^T / \sqrt{\hat{c}}$, with \hat{c} the feature dimension. We then follow [36] to append a stack row and column to $\hat{\mathbf{S}}_l$ filled with a learnable parameter α , and iteratively run the Sinkhorn Algorithm [37] on it, yielding a normalized similarity matrix $\bar{\mathbf{C}}_l$. By removing the slack row and entry of $\bar{\mathbf{C}}_l$ we obtain the confidence matrix $\hat{\mathbf{C}}_l$, from which the mutual top- k entries, *i.e.*, entries with top- k confidence on both the row and the column, are selected to formulate a point correspondence set \mathcal{C}_l . The final correspondence set \mathcal{C} is collected by $\mathcal{C} = \cup_{l=1}^{|\mathcal{C}'|} \mathcal{C}_l$.

Loss Function. Our loss function reads as $\mathcal{L} = \mathcal{L}_s + \lambda \mathcal{L}_p$, with a superpoint matching loss \mathcal{L}_s and a point matching loss \mathcal{L}_p balanced by a hyper-parameter λ ($\lambda = 1$ by default). The detailed definition is introduced in the Appendix.

4. Experiment

We evaluate RoITr on both rigid (3DMatch [52] & 3DLoMatch [19]) and non-rigid (4DMatch [21] & 4DLoMatch [21]) benchmarks. For the rigid matching, we further evaluate our correspondences on the registration task, where RANSAC [12] is used for pose estimation. Implementation details are introduced in the Appendix.

4.1. Rigid Indoor Scenes: 3DMatch & 3DLoMatch

Dataset. 3DMatch [52] collects 62 indoor scenes, among which 46 are used for training, 8 for validation, and 8 for testing. We use the data processed by [19] where the 3DMatch data is spilt as 3DMatch ($> 30\%$ overlap) and 3DLoMatch (10% \sim 30% overlap). To evaluate robustness to arbitrary rotations, we follow [49] for creating the rotated benchmarks, where full-range rotations are individually added to the two frames of each point cloud pair.

Metrics. We follow [19] to use three metrics for evaluation: (1). *Inlier Ratio* (IR) that computes the ratio of putative correspondences whose residual distance is smaller than a threshold (*i.e.*, 0.1m) under the ground-truth transformation; (2). *Feature Matching Recall* (FMR) that calculates the fraction of point cloud pairs whose IR is larger than a threshold (*i.e.*, 5%); (3). *Registration Recall* (RR)¹

¹We follow [49] to calculate the RR strictly with RMSE $< 0.2\text{m}$ on the rotated data, which is slightly different from the RR on the original data.

# Samples=5,000	3DMatch		3DLoMatch	
	Origin	Rotated	Origin	Rotated
<i>Feature Matching Recall (%)</i> \uparrow				
SpinNet [1]	97.4	97.4	75.5	75.2
Predator [19]	96.6	96.2	78.6	73.7
CoFiNet [50]	98.1	97.4	83.1	78.6
YOHO [44]	98.2	97.8	79.4	77.8
RIGA [49]	97.9	98.2	85.1	84.5
Lepard [21]	98.0	97.4	83.1	79.5
GeoTrans [29]	97.9	97.8	<u>88.3</u>	<u>85.8</u>
RoITr (Ours)	98.0	98.2	89.6	89.4
<i>Inlier Ratio (%)</i> \uparrow				
SpinNet [1]	48.5	48.7	25.7	25.7
Predator [19]	58.0	52.8	26.7	22.4
CoFiNet [50]	49.8	46.8	24.4	21.5
YOHO [44]	64.4	64.1	25.9	23.2
RIGA [49]	68.4	<u>68.5</u>	32.1	32.1
Lepard [21]	58.6	53.7	28.4	24.4
GeoTrans [29]	<u>71.9</u>	68.2	<u>43.5</u>	<u>40.0</u>
RoITr (Ours)	82.6	82.3	54.3	53.2
<i>Registration Recall (%)</i> \uparrow				
SpinNet [1]	88.8	93.2	58.2	61.8
Predator [19]	89.0	92.0	59.8	58.6
CoFiNet [50]	89.3	92.0	67.5	62.5
YOHO [44]	90.8	92.5	65.2	66.8
RIGA [49]	89.3	93.0	65.1	66.9
Lepard [21]	92.7	84.9	65.4	49.0
GeoTrans [29]	92.0	92.0	75.0	71.8
RoITr (Ours)	91.9	94.7	<u>74.8</u>	77.2

Table 1. Quantitative results on (Rotated) 3DMatch & 3DLoMatch. 5,000 points/correspondences are used for the evaluation.

that counts the fraction of point cloud pairs that are correctly registered (*i.e.*, with RMSE $< 0.2\text{m}$). See the Appendix for the detailed definition.

Comparison with the State-of-the-Art. We compare RoITr with 7 state-of-the-art methods, among which Predator [19], CoFiNet [50], Lepard [21], and GeoTrans [29] are rotation-sensitive models, while SpinNet [1], YOHO [44], and RIGA [49] guarantee the rotation invariance by design. In Tab. 1 we demonstrate the matching and registration results on 3DMatch and 3DLoMatch, as well as on their rotated versions, with 5,000 sampled points/correspondences. Regarding IR, RoITr outperforms all the others by a large margin on both datasets, which indicates our method matches points more correctly. For FMR, we significantly surpass all the others on 3DLoMatch, while staying on par with CoFiNet and YOHO on 3DMatch, which indicates that our model is good at coping with hard cases, *i.e.*, we find at least 5% inliers on more test data. For the registration evaluation in terms of RR, RoITr achieves comparable performance with GeoTrans and Lepard on 3DMatch, but leads the board together with GeoTrans on 3DLoMatch with an overwhelming advantage over the others. Our stability against additional rotations is further demonstrated on the rotated data, where we outperform all the others with a substantial margin. Qualitative results can be found in Fig. 5.

Analysis on the Number of Correspondences. We fur-

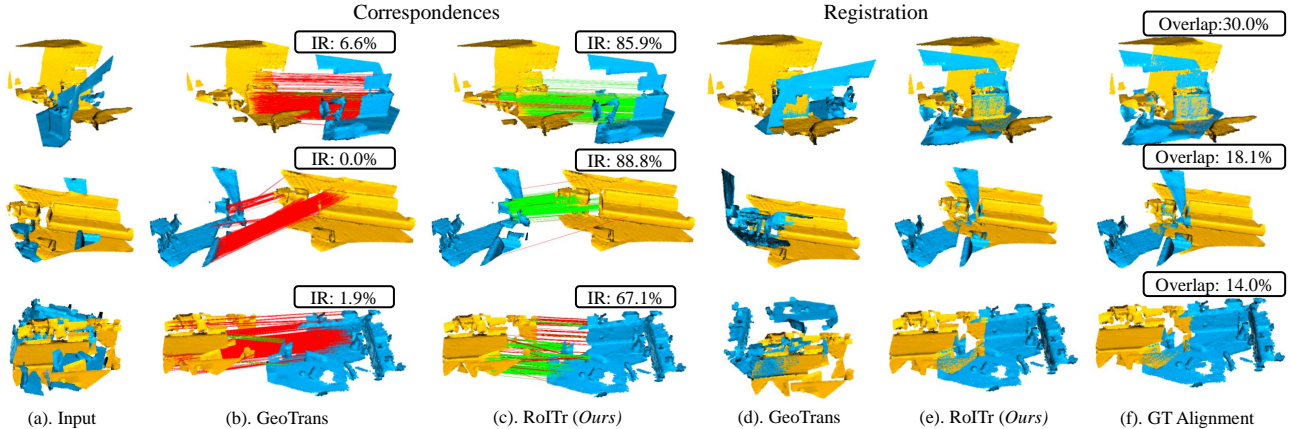


Figure 5. Qualitative results on 3DLoMatch. GeoTrans [29] is used as the baseline. Columns (b) and (c) show the correspondences, while columns (d) and (e) demonstrate the registration results. Green/red lines indicate inliers/outliers. More cases are shown in the Appendix.

# Samples	3DMatch					3DLoMatch				
	5000	2500	1000	500	250	5000	2500	1000	500	250
Feature Matching Recall (%) ↑										
SpinNet [1]	97.4	97.0	96.4	96.7	94.8	75.5	75.1	74.2	69.0	62.7
Predator [19]	96.6	96.6	96.5	96.3	96.5	78.6	77.4	76.3	75.7	75.3
CoFiNet [50]	<u>98.1</u>	98.3	98.1	98.2	98.3	83.1	83.5	83.3	83.1	82.6
YOHO [44]	98.2	97.6	97.5	97.7	96.0	79.4	78.1	76.3	73.8	69.1
RIGA [49]	97.9	97.8	97.7	97.7	97.6	85.1	85.0	85.1	84.3	85.1
GeoTrans [29]	97.9	97.9	<u>97.9</u>	97.9	97.6	<u>88.3</u>	<u>88.6</u>	<u>88.8</u>	<u>88.6</u>	<u>88.3</u>
RoITr (Ours)	98.0	<u>98.0</u>	<u>97.9</u>	<u>98.0</u>	<u>97.9</u>	89.6	89.6	89.5	89.4	89.3
Inlier Ratio (%) ↑										
SpinNet [1]	48.5	46.2	40.8	35.1	29.0	25.7	23.7	20.6	18.2	13.1
Predator [19]	58.0	58.4	57.1	54.1	49.3	26.7	28.1	28.3	27.5	25.8
CoFiNet [50]	49.8	51.2	51.9	52.2	52.2	24.4	25.9	26.7	26.8	26.9
YOHO [44]	64.4	60.7	55.7	46.4	41.2	25.9	23.3	22.6	18.2	15.0
RIGA [49]	68.4	69.7	70.6	70.9	71.0	32.1	33.4	34.3	34.5	34.6
GeoTrans [29]	<u>71.9</u>	<u>75.2</u>	<u>76.0</u>	<u>82.2</u>	85.1	<u>43.5</u>	<u>45.3</u>	<u>46.2</u>	<u>52.9</u>	57.7
RoITr (Ours)	82.6	82.8	83.0	83.0	<u>83.0</u>	54.3	54.6	55.1	55.2	<u>55.3</u>
Registration Recall (%) ↑										
SpinNet [1]	88.8	88.0	84.5	79.0	69.2	58.2	56.7	49.8	41.0	26.7
Predator [19]	89.0	89.9	90.6	88.5	86.6	59.8	61.2	62.4	60.8	58.1
CoFiNet [50]	89.3	88.9	88.4	87.4	87.0	67.5	66.2	64.2	63.1	61.0
YOHO [44]	90.8	90.3	89.1	88.6	84.5	65.2	65.5	63.2	56.5	48.0
RIGA [49]	89.3	88.4	89.1	89.0	87.7	65.1	64.7	64.5	64.1	61.8
GeoTrans [29]	92.0	91.8	91.8	91.4	91.2	75.0	74.8	<u>74.2</u>	<u>74.1</u>	<u>73.5</u>
RoITr (Ours)	<u>91.9</u>	<u>91.7</u>	91.8	91.4	<u>91.0</u>	<u>74.7</u>	74.8	74.8	74.2	73.6

Table 2. Quantitative results on 3DMatch & 3DLoMatch with a varying number of points/correspondences. See the results on rotated data in the Appendix.

ther analyze the influence of a varying number of correspondences. As illustrated in Tab. 2, RoITr shows outstanding performance on both datasets with various correspondences, proving its stability when only a few correspondences are accessible. The same test on the rotated benchmarks is given in the Appendix.

4.2. Deformable Objects: 4DMatch & 4DLoMatch

Dataset. 4DMatch [21] contains 1,761 animations randomly selected from DeformingThings4D [22]. The 1,761 sequences are divided into 1,232/176/353 as train/val/test, where the test set is further split into 4DMatch and 4DLoMatch based on an overlap ratio threshold of 45%.

Metrics. We follow [21] to use two different metrics: (1). *Inlier Ratio* (IR) which is defined as same as the IR on 3DMatch, but with a different threshold (*i.e.*, 0.04m);

(2). *Non-rigid Feature Matching Recall* (NFMR) that measures the fraction of ground-truth matches that can be successfully recovered by the putative correspondences. The details of the metrics are given in the Appendix.

Category	Method	4DMatch		4DLoMatch	
		NFMR(%) ↑	IR(%) ↑	NFMR(%) ↑	IR(%) ↑
Scene Flow	PWC [45]	21.6	20.0	10.0	7.2
	FLOT [26]	27.1	24.9	15.2	10.7
Feature Matching	Predator [19]	56.4	60.4	32.1	27.5
	GeoTrans [29]	<u>83.2</u>	82.2	65.4	<u>63.6</u>
	Lepard [21]	83.7	<u>82.7</u>	66.9	55.7
	RoITr (Ours)	83.0	84.4	69.4	67.6

Table 3. Quantitative results on 4DMatch & 4DLoMatch.

Comparison with the State-of-the-Art. We compare RoITr with 5 baselines, among which PWC [45] and FLOT [26] are scene flow-based methods, while Predator [19], Lepard [21], GeoTrans [29] are based on feature matching. The results shown in Tab. 3 indicate that although our rotation-invariance is mainly designed for rigid scenarios, RoITr could also achieve outstanding performance in the non-rigid matching task, which further confirms the superiority of our model design. Qualitative results are demonstrated in Fig. 6.

4.3. Ablation Study

Local Attention. We first replace our PPFTrans with Point-Transformer (PT) [54] in Tab. 4 (a.1), which leads to a sharp performance drop. We then ablate by embedding our PPF-based local coordinates into PT (Tab. 4 (a.2)) and by adopting the relative coordinates, *i.e.*, $\mathbf{p}_j - \mathbf{p}_j$, used by PT in our PAM (Tab. 4 (a.3)). Our local coordinate representation significantly boosts the performance of PT in the task of point cloud matching and meanwhile makes it rotation-invariant, although its performance is still far behind ours. However, the relative coordinates fail to work in our PAM, as we adopt a more efficient attention mechanism [43] that learns a scalar attention value for each feature $\mathbf{x} \in \mathbb{R}^c$ and is consequently hard to work under varying poses with a

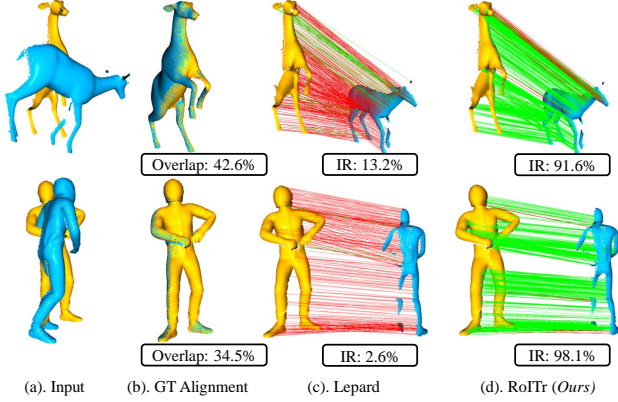


Figure 6. Qualitative results of non-rigid matching on 4DLoMatch with Leopard [21] as the baseline. Green/red lines indicate inliers/outliers. See the Appendix for more examples.

rotation-sensitive design. As a comparison, PT learns a per-channel vector attention $\mathbf{a} \in \mathbb{R}^c$ for the same feature \mathbf{x} and could deal with the pose variations, but at the cost of the efficiency as shown in Fig. 7. When the number of channels is increased, our advantage in terms of efficiency is enlarged. As we achieve that with more parameters, the gap becomes more significant when runtime is normalized with the number of parameters in the right figure. With our PPF-based local coordinate, the scalar attention could focus on the pose-agnostic pure geometry and therefore achieves the best performance shown in Tab. 4 (a.4).

Abstraction Layer. We ablate our Attentional Abstraction Layer (AAL) by replacing it with the pooling-based abstraction design used in [27, 28, 54]. We test the max pooling in Tab. 4 (b.1) and the average pooling in Tab. 4 (b.2), both showing a degrading performance compared with our AAL, which demonstrates our superiority.

Backbone. In Tab. 4 (a.1) we have shown our superiority compared with PT [54]. We further replace our PPFTrans with the KPConv-based backbone network which is widely used in previous deep matchers [19, 29, 50]. The fact that KPConv falls behind our design demonstrates the advantage of PPFTrans in geometry encoding.

Global Transformer. We replace our design with the global transformer of GeoTrans [29] which performs state-of-the-art but without the cross-frame spatial awareness. The dropping results in Tab. 4 (d.1) proves the excellence of our design with the cross-frame position awareness.

The Number of Global Transformers. To demonstrate the importance of being globally aware, we first remove the global transformer. The substantial performance drop confirms the significance of global awareness. Then we add one global transformer and observe an increased performance. In our default setting with 3 global transformers, the model performs the best. However, when the number is increased to 5, the model shows a slight performance drop, which we owe to overfitting. As the data augmentation of rotations

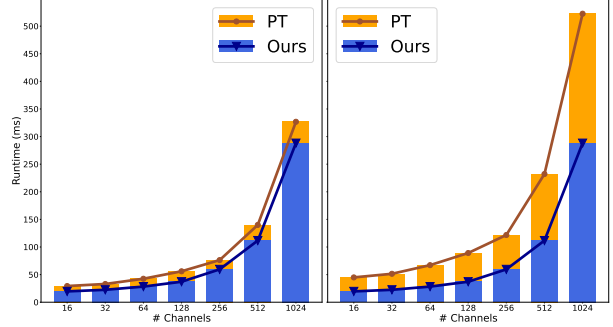


Figure 7. **Left:** Runtime comparison between our PPF attention Module (PAM) and the local attention in PointTransformer [54]. **Right:** Runtime normalized by aligning the number of parameters.

has less effect on an intrinsically rotation-invariant method, more data is required for training a larger model.

Category	Model	Origin			Rotated		
		FMR	IR	RR	FMR	IR	RR
a. Local	1. PT [54]	79.0	36.5	61.6	76.5	34.7	60.0
	*2. PPF+PT [54]	87.0	49.9	69.9	86.8	49.4	71.2
	3. Δxyz +Ours	-	-	-	-	-	-
	*4. Ours	89.6	54.3	74.7	89.4	53.2	77.2
b. Aggregation	*1. max pooling	85.2	50.1	70.5	85.4	50.2	71.9
	*2. avg pooling	87.8	52.6	73.8	87.2	52.5	74.7
	*3. Ours	89.6	54.3	74.7	89.4	53.2	77.2
c. Backbone	1. KPConv [40]	85.2	44.4	70.6	83.0	42.3	71.5
	*2. Ours	89.6	54.3	74.7	89.4	53.2	77.2
d. Global	*1. GeoTrans [29]	87.7	53.6	73.0	87.5	53.2	75.1
	*2. Ours	89.6	54.3	74.7	89.4	53.2	77.2
e. #Global	*1. $g = 0$	87.2	37.6	70.7	87.5	37.6	72.7
	*2. $g = 1$	87.1	42.1	70.8	86.8	42.1	73.0
	*3. $g = 3$ (Ours)	89.6	54.3	74.7	89.4	53.2	77.2
	*4. $g = 5$	87.1	52.5	72.1	87.0	52.4	73.3

Table 4. Ablation study on (rotated) 3DLoMatch. 5,000 points/correspondences are leveraged. * indicates the methods with intrinsic rotation invariance. See the Appendix for the results on (rotated) 3DMatch.

5. Conclusion

We introduce RoITr - an intrinsically rotation-invariant model for point cloud matching. We proposed PAM (PPF Attention Module) that embeds PPF-based local coordinates to encode rotation-invariant local geometry. This module lies at the core of AAL (Attention Abstraction Layer), PAL (PPF Attention Layer), and TUL (Transition Up Layer) which are consecutively stacked to compose PPFTrans (PPF Transformer) for highly-representative and pose-agnostic geometry description. We further enhanced features with the global context by introducing a novel global transformer architecture, which ensures the rotation-invariant cross-frame spatial awareness. Extensive experiments are conducted on both rigid and non-rigid benchmarks to demonstrate the superiority of our approach, especially the remarkable robustness against arbitrary rotations. However, as RoITr does not explicitly handle the occlusion, it may fail in cases with extremely limited overlap. We further discuss limitations in the Appendix. In the future, we would like to incorporate RGB information to cope with symmetric structures.

A. Appendix

In this appendix, we first provide the implementation details in Sec. A.1. Then the network architecture is detailed in Sec. A.2. Moreover, the detailed definition of the geometric embedding, the loss function, and the evaluation metrics are illustrated in Sec. A.3, Sec. A.4, and Sec. A.5, respectively. Furthermore, more quantitative and qualitative results are demonstrated in Sec. A.6 and Sec. A.7, respectively. Finally, the runtime is first analyzed in Sec. A.8, and the limitations are further discussed in Sec. A.9.

A.1. Implementation Details

We implement RoITr with PyTorch [25]. The matching model can be trained end-to-end on a single Nvidia RTX 3090 with 24G memory. In practice, we train the model on-parallel using $4 \times$ Nvidia 3090 GPUs for ~ 35 epochs on both 3DMatch/3DLoMatch [19, 52] and 4DMatch/4DLoMatch [21]. It takes ~ 35 hours and ~ 30 hours for full convergence on 3DMatch/3DLoMatch and 4DMatch/4DLoMatch, respectively. The batch size is set to 1. We use an Adam optimizer [20] with an initial learning rate of $1e-4$, which is exponentially decayed by 0.05 after each epoch. On 3DMatch/3DLoMatch, we select $|C'| = 256$ superpoint correspondences with the highest scores. Based on each superpoint correspondence, we further extract the mutual top-3 point correspondences whose confidence scores are larger than 0.05 as the point correspondences. For non-rigid matching, we first pick the superpoint correspondences whose Euclidean distance is smaller than 0.75 (pick the top-128 instead if the number of selected correspondences is smaller than 128) and extract the mutual top-2 point correspondences with scores larger than 0.05.

A.2. Network Architecture

PPFTrans Encoder-Decoder. We detail the architecture of PPFTrans in Tab. 5. The encoder part has $4 \times$ encoder blocks. In each block, AAL first downsamples the points and aggregates the information in a local vicinity. PAL further enhances the features with both the pose-agnostic local geometry and highly-representative learned context. The decoder part also comprises $4 \times$ decoder blocks. In each block (except for Block₄), TUL first subsamples the points and incorporates the information flowing from the encoder via skip connections. The obtained features are further enhanced by the following PAL.

Global Transformer. The details of the global transformer are demonstrated in Tab. 6. It has $3 \times$ transformer blocks, each comprising a geometry-aware self-attention module (GSM) followed by a position-aware cross-attention module (PCM). In each transformer block, GSM first aggregates the global context individually for

each point cloud. Then in PCM, the global context flows from the second frame to the first one and then from the first frame to the second one.

Feed-Forward Network. The structure of the feed-forward network is illustrated in Fig. 8. It details the feed-forward network in the context branch of GSM in Fig. 4 of the main paper.

A.3. Geometric Embedding

Taking superpoints $\mathbf{P}' \in \mathbb{R}^{n' \times 3}$ as an instance, the geometric embedding $\mathbf{G}'_P \in \mathbb{R}^{n' \times n' \times c'}$ proposed in [29] depicts the pairwise geometric relationship among superpoints in a rotation-invariant fashion. It comprises a distance-based part $\mathbf{G}'_D \in \mathbb{R}^{n' \times n' \times c'}$ as well as an angle-based part $\mathbf{G}'_A \in \mathbb{R}^{n' \times n' \times 3 \times c'}$.

Euclidean Distance. The pairwise Euclidean distance is defined as $\rho_{i,j} = \|\mathbf{p}'_i - \mathbf{p}'_j\|_2$, which is projected to a c' -dimension (note that c' must be an even number) embedding via the sinusoidal function [43]:

$$\begin{cases} \mathbf{G}'_D(i, j, 2l + 1) = \sin\left(\frac{\rho_{i,j}/\sigma_d}{10000^{2l/c'}}\right), \\ \mathbf{G}'_D(i, j, 2l + 2) = \cos\left(\frac{\rho_{i,j}/\sigma_d}{10000^{2l/c'}}\right), \end{cases} \quad (11)$$

with $0 \leq l < c'/2$ and $\sigma_d = 0.2$.

Angles. Given a superpoint pair $(\mathbf{p}'_i, \mathbf{p}'_j)$, the 3-nearest neighbors of \mathbf{p}'_i w.r.t. \mathbf{P}' is first retrieved and denoted as $\mathcal{N}(i)$. For each $k \in \mathcal{N}(i)$, we calculate the angle between two vectors by $\alpha_{i,j}^k = \angle(\mathbf{p}'_k - \mathbf{p}'_i, \mathbf{p}'_j - \mathbf{p}'_i)$ [5, 10], upon which the c' -dimension angle-based embedding is defined as:

$$\begin{cases} \mathbf{G}'_A(i, j, k, 2l + 1) = \sin\left(\frac{\alpha_{i,j}^k/\sigma_a}{10000^{2l/c'}}\right), \\ \mathbf{G}'_A(i, j, k, 2l + 2) = \cos\left(\frac{\alpha_{i,j}^k/\sigma_a}{10000^{2l/c'}}\right), \end{cases} \quad (12)$$

with $0 \leq l < c'/2$ and $\sigma_a = 15$.

The pairwise geometric embedding \mathbf{G}'_P finally reads as:

$$\mathbf{G}'_P = \mathbf{G}'_D \mathbf{W}_D + \max_k(\mathbf{G}'_A \mathbf{W}_A), \quad (13)$$

where $\max_k(\mathbf{G}'_A \mathbf{W}_A)$ indicates the max-pooling operation over the second last dimension, and $\mathbf{W}_D, \mathbf{W}_A \in \mathbb{R}^{c' \times c'}$ stand for two learnable matrices.

A.4. Loss Function

Superpoint Matching Loss. We use the Circle Loss [39] for superpoint matching. Following [29], we use the overlap ratio between the vicinity of superpoints to weigh different ground truth superpoint correspondences. More specifically, for each superpoint $\mathbf{p}'_i \in \mathbf{P}'$ with an associated feature $\tilde{\mathbf{x}}'_i$ (unit vector after normalization), we sample a positive set of superpoints from \mathbf{Q}' , denoted as $\mathcal{E}'_i = \{\mathbf{q}'_j \in$

Stage	Block	Operation
Input		$\mathcal{P} = (\mathbf{P}, \mathbf{N}, \mathbf{X} \in \mathbb{R}^{n \times 1})$
Encoder	$\text{Block}_1^e(\mathcal{P}) \rightarrow \mathcal{P}_1$	$\text{AAL}(n \times 1) \rightarrow n \times 64$ $\text{PAL}(n \times 64) \rightarrow n \times 64$
	$\text{Block}_2^e(\mathcal{P}_1) \rightarrow \mathcal{P}_2$	$\text{AAL}(n \times 64) \rightarrow n/4 \times 128$ $\text{PAL}(n/4 \times 128) \rightarrow n/4 \times 128$
	$\text{Block}_3^e(\mathcal{P}_2) \rightarrow \mathcal{P}_3$	$\text{AAL}(n/4 \times 128) \rightarrow n/16 \times 256$ $\text{PAL}(n/16 \times 256) \rightarrow n/16 \times 256$
	$\text{Block}_4^e(\mathcal{P}_3) \rightarrow \mathcal{P}'$	$\text{AAL}(n/16 \times 256) \rightarrow n/64 \times 256$ $\text{PAL}(n/64 \times 256) \rightarrow n/64 \times 256$
Decoder	$\text{Block}_4^d(\mathcal{P}') \rightarrow \hat{\mathcal{P}}_4$	$\text{TUL}(n/64 \times 256) \rightarrow n/64 \times 256$ $\text{PAL}: n/64 \times 256 \rightarrow n/64 \times 256$
	$\text{Block}_3^d(\hat{\mathcal{P}}_4, \mathcal{P}_3) \rightarrow \hat{\mathcal{P}}_3$	$\text{TUL}(n/64 \times 256, n/16 \times 256) \rightarrow n/16 \times 256$ $\text{PAL}(n/16 \times 256) \rightarrow n/16 \times 256$
	$\text{Block}_2^d(\hat{\mathcal{P}}_3, \mathcal{P}_2) \rightarrow \hat{\mathcal{P}}_2$	$\text{TUL}(n/16 \times 256, n/4 \times 128) \rightarrow n/4 \times 128$ $\text{PAL}(n/4 \times 128) \rightarrow n/4 \times 128$
	$\text{Block}_1^d(\hat{\mathcal{P}}_2, \mathcal{P}_1) \rightarrow \hat{\mathcal{P}}$	$\text{TUL}(n/4 \times 128, n \times 64) \rightarrow n \times 64$ $\text{PAL}(n \times 64) \rightarrow n \times 64$
Output		$\mathcal{P}' = (\mathbf{P}', \mathbf{N}', \mathbf{X}')$; $\hat{\mathcal{P}} = (\hat{\mathbf{P}}, \hat{\mathbf{N}}, \hat{\mathbf{X}})$

Table 5. Detailed architecture of the PPFTrans encoder-decoder.

Block	Module	Operation
Input		$\mathcal{P}' = (\mathbf{P}', \mathbf{N}', \mathbf{X}')$ $\mathcal{Q}' = (\mathbf{Q}', \mathbf{M}', \mathbf{Y}')$
Trans ₁	$\text{Self}_1(\mathcal{P}') \rightarrow \tilde{\mathcal{P}}'_1$ $\text{Self}_1(\mathcal{Q}') \rightarrow \tilde{\mathcal{Q}}'_1$	$\text{GSM}(n' \times c') \rightarrow n' \times c'$ $\text{GSM}(m' \times c') \rightarrow m' \times c'$
	$\text{Cross}_1(\tilde{\mathcal{P}}'_1, \tilde{\mathcal{Q}}'_1) \rightarrow \mathcal{P}'_1$	$\text{PCM}(n' \times c', m' \times c') \rightarrow n' \times c'$
	$\text{Cross}_1(\tilde{\mathcal{Q}}'_1, \mathcal{P}'_1) \rightarrow \mathcal{Q}'_1$	$\text{PCM}(m' \times c', n' \times c') \rightarrow m' \times c'$
Trans ₂	$\text{Self}_2(\mathcal{P}'_1) \rightarrow \tilde{\mathcal{P}}'_2$ $\text{Self}_2(\mathcal{Q}'_1) \rightarrow \tilde{\mathcal{Q}}'_2$	$\text{GSM}(n' \times c') \rightarrow n' \times c'$ $\text{GSM}(m' \times c') \rightarrow m' \times c'$
	$\text{Cross}_2(\tilde{\mathcal{P}}'_2, \tilde{\mathcal{Q}}'_2) \rightarrow \mathcal{P}'_2$	$\text{PCM}(n' \times c', m' \times c') \rightarrow n' \times c'$
	$\text{Cross}_2(\tilde{\mathcal{Q}}'_2, \mathcal{P}'_2) \rightarrow \mathcal{Q}'_2$	$\text{PCM}(m' \times c', n' \times c') \rightarrow m' \times c'$
Trans ₃	$\text{Self}_3(\mathcal{P}'_2) \rightarrow \tilde{\mathcal{P}}'_3$ $\text{Self}_3(\mathcal{Q}'_2) \rightarrow \tilde{\mathcal{Q}}'_3$	$\text{GSM}(n' \times c') \rightarrow n' \times c'$ $\text{GSM}(m' \times c') \rightarrow m' \times c'$
	$\text{Cross}_3(\tilde{\mathcal{P}}'_3, \tilde{\mathcal{Q}}'_3) \rightarrow \mathcal{P}'_3$	$\text{PCM}(n' \times c', m' \times c') \rightarrow n' \times c'$
	$\text{Cross}_3(\tilde{\mathcal{Q}}'_3, \mathcal{P}'_3) \rightarrow \mathcal{Q}'_3$	$\text{PCM}(m' \times c', n' \times c') \rightarrow m' \times c'$
Output		$\tilde{\mathcal{P}}' = (\mathbf{P}', \mathbf{N}', \tilde{\mathbf{X}}')$ $\tilde{\mathcal{Q}}' = (\mathbf{Q}', \mathbf{M}', \tilde{\mathbf{Y}}')$

Table 6. Detailed architecture of the global transformer.

$\mathbf{Q}' \{ \mathcal{O}(\mathbf{p}'_i, \mathbf{q}'_j) > \tau_r \}$, where \mathcal{O} is the function that calculates the overlap ratio between the vicinity of two superpoints, and τ_r is the threshold to select positive samples ($\tau_r=0.1$ by default). The overlap ratio function is defined as:

$$\mathcal{O}(\mathbf{p}'_i, \mathbf{q}'_j) = \frac{|\{ \hat{\mathbf{p}}_u \in \hat{\mathbf{G}}_i^P | \exists \hat{\mathbf{q}}_v \in \hat{\mathbf{G}}_j^Q \text{ s.t. } \hat{\mathbf{p}}_u \Leftrightarrow \hat{\mathbf{q}}_v \}|}{|\{ \hat{\mathbf{p}}_u \in \hat{\mathbf{G}}_i^P \}|}, \quad (14)$$

where \Leftrightarrow denotes the correspondence relationship and $\hat{\mathbf{G}}_i^P$ is the group of points from $\hat{\mathbf{P}}$ assigned to \mathbf{p}'_i by the Point-to-Node grouping strategy [50].

We further sample a negative set of superpoints $\mathcal{F}_i^P =$

$\{ \mathbf{q}'_j \in \mathbf{Q}' | \mathcal{O}(\mathbf{p}'_i, \mathbf{q}'_j) = 0 \}$. Then for \mathbf{P}' , the superpoint matching loss is computed as:

$$\mathcal{L}_c^P = \frac{1}{n'} \sum_{i=1}^{n'} \log[1 + \sum_{\mathbf{q}'_j \in \mathcal{E}_i^P} e^{r_i^j \beta_e^{i,j} (d_i^j - \Delta_e)} \cdot \sum_{\mathbf{q}'_k \in \mathcal{F}_i^P} e^{\beta_f^{i,k} (\Delta_f - d_i^k)}], \quad (15)$$

with $r_i^j := \mathcal{O}(\mathbf{p}'_i, \mathbf{q}'_j)$ and $d_i^j = \|\tilde{\mathbf{x}}'_i - \tilde{\mathbf{y}}'_j\|_2$. Moreover, Δ_e and Δ_f are the positive and negative margins ($\Delta_e=0.1$

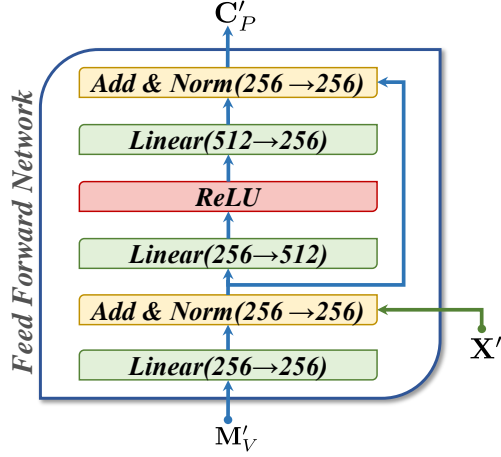


Figure 8. Detailed architecture of the feed-forward network. LayerNorm [2] is used for normalization.

and $\Delta_f=1.4$ by default). $\beta_e^{i,j} = \gamma(d_i^j - \Delta_e)$ and $\beta_f^{i,k} = \gamma(\Delta_f - d_i^k)$ are the weights individually determined for different samples, with γ a hyper-parameter. The same loss for \mathbf{Q}' is defined in a similar way, and the overall loss reads as $\mathcal{L}_s = (\mathcal{L}_s^P + \mathcal{L}_s^Q)/2$.

Point Matching Loss. For each superpoint correspondence $\mathcal{C}'_l = (\mathbf{p}'_i, \mathbf{q}'_j) \in \mathcal{C}'$, we adopt a negative log-likelihood loss [36] on its corresponding normalized similarity matrix $\overline{\mathbf{C}}_l \in \mathbb{R}^{(\overline{n}+1) \times (\overline{m}+1)}$. We define $\mathcal{M}_l = \{(u, v) | \hat{\mathbf{p}}_u \Leftrightarrow \hat{\mathbf{q}}_v \text{ with } \hat{\mathbf{p}}_u \in \hat{\mathbf{G}}_i^P, \hat{\mathbf{q}}_v \in \hat{\mathbf{G}}_j^Q\}$ as the set comprising the indices of corresponding points. We further define $\mathcal{I}_l = \{u | \hat{\mathbf{p}}_u \nleftrightarrow \hat{\mathbf{q}}_v, \forall \hat{\mathbf{q}}_v \in \hat{\mathbf{G}}_j^Q\}$ and $\mathcal{J}_l = \{v | \hat{\mathbf{q}}_v \nleftrightarrow \hat{\mathbf{p}}_u, \forall \hat{\mathbf{p}}_u \in \hat{\mathbf{G}}_i^P\}$ as the sets of indices of points that have no correspondence in the opposite frame, with \nleftrightarrow depicting non-correspondence relationship. Then the point matching loss on \mathcal{C}'_l can be defined as:

$$\mathcal{L}_f^l = - \sum_{(u,v) \in \mathcal{M}_l} \log \overline{c}_{u,v}^l - \sum_{u \in \mathcal{I}_l} \log \overline{c}_{u,\overline{m}+1}^l - \sum_{v \in \mathcal{J}_l} \log \overline{c}_{\overline{n}+1,v}^l, \quad (16)$$

where $\overline{c}_{u,v}^l := \overline{\mathbf{C}}_l(u, v)$ stands for the entry on the u^{th} row and v^{th} column of $\overline{\mathbf{C}}_l$. The overall point matching loss reads as $\mathcal{L}_p = \frac{1}{|\mathcal{C}'|} \sum_{l=1}^{|\mathcal{C}'|} \mathcal{L}_f^l$.

A.5. Detailed Metrics

Given a point cloud pair $\mathbf{P} \in \mathbb{R}^{n \times 3}$ and $\mathbf{Q} \in \mathbb{R}^{m \times 3}$, RoITr generates a correspondence set \mathcal{C} by matching the downsampled point cloud pair $\hat{\mathbf{P}} \in \mathbb{R}^{\hat{n} \times 3}$ and $\hat{\mathbf{Q}} \in \mathbb{R}^{\hat{m} \times 3}$. We detail all the metrics for evaluation hereafter.

Inlier Ratio (IR). IR counts the fraction of putative correspondences $(\hat{\mathbf{p}}_u, \hat{\mathbf{q}}_v) \in \mathcal{C}$ whose Euclidean distance is under a threshold τ_1 (0.1m on 3DMatch/3DLoMatch, 0.04m on 4DMatch/4DLoMatch) under the ground-truth transformation \mathbf{T}^* :

$$\mathcal{I}(\mathcal{C} | \mathbf{T}^*) = \frac{1}{|\mathcal{C}|} \sum_{(\hat{\mathbf{p}}_u, \hat{\mathbf{q}}_v) \in \mathcal{C}} \mathbb{1}(\|\mathbf{T}^*(\hat{\mathbf{p}}_u) - \hat{\mathbf{q}}_v\|_2 < \tau_1), \quad (17)$$

with $\mathbb{1}(\cdot)$ the indicator function.

Feature Matching Recall (FMR). FMR counts the fraction of point cloud pairs whose IR is larger than a threshold $\tau_2 = 0.05$:

$$\mathcal{F}(\mathcal{T}) = \frac{1}{|\mathcal{T}|} \sum_{t=1}^{|\mathcal{T}|} \mathbb{1}(\mathcal{I}(\mathcal{C}_t | \mathbf{T}_t^*) > \tau_2), \quad (18)$$

with \mathcal{T} the testing set and \mathcal{T}_t the t^{th} point cloud pair in the dataset.

Registration Recall (RR). RR computes the fraction of point cloud pairs that are registered correctly based on the putative correspondences, measured by the *Root-Mean-Square Error* (RMSE). Following [19], we define RMSE on the original 3DMatch/3DLoMatch as:

$$\mathcal{R}_1(\mathcal{C} | \mathcal{C}^*) = \sqrt{\frac{1}{|\mathcal{C}^*|} \sum_{(\mathbf{p}_i, \mathbf{q}_j) \in \mathcal{C}^*} \|\mathbf{T}(\mathbf{p}_i) - \mathbf{q}_j\|_2^2}, \quad (19)$$

with \mathcal{C}^* the ground-truth correspondence set established upon \mathbf{P} and \mathbf{Q} , and \mathbf{T} the transformation estimated based on \mathcal{C} . On Rotated 3DMatch/3DLoMatch, we follow [49, 51] and define the RMSE as:

$$\mathcal{R}_2(\mathcal{C} | \mathbf{T}^*, \mathbf{P}) \approx \frac{1}{n} \sqrt{\sum_{\mathbf{p}_i \in \mathbf{P}} \|\mathbf{T}(\mathbf{p}_i) - \mathbf{T}^*(\mathbf{p}_i)\|_2^2}, \quad (20)$$

with \mathbf{T} the transformation estimated based on \mathcal{C} and \mathbf{T}^* the ground-truth transformation. RR is finally calculated as:

$$\mathcal{R}(\mathcal{T}) = \frac{1}{|\mathcal{T}|} \sum_{t=1}^{\mathcal{T}} \mathbb{1}(\mathcal{R}_1(\mathcal{C} | \mathcal{C}^*) < \tau_3) \quad \text{or} \quad (21)$$

$$\frac{1}{|\mathcal{T}|} \sum_{t=1}^{\mathcal{T}} \mathbb{1}(\mathcal{R}_2(\mathcal{C} | \mathbf{T}^*, \mathbf{P})) < \tau_3),$$

with $\tau_3 = 0.2\text{m}$.

Non-Rigid Feature Matching Recall (NFMR). NFMR counts the fraction of ground-truth correspondences \mathcal{C}^* that can be recovered by the putative correspondences \mathcal{C} . The deformation flow $\hat{\mathbf{d}}_u$ for each putative correspondence $(\hat{\mathbf{p}}_u, \hat{\mathbf{q}}_v) \in \mathcal{C}$ is defined as $\hat{\mathbf{d}}_u = \hat{\mathbf{q}}_v - \hat{\mathbf{p}}_u$. Then for each $(\mathbf{p}_i, \mathbf{q}_j) \in \mathcal{C}^*$, the deformation flow can be computed via interpolation:

$$\mathbf{d}_i = \frac{\sum_{u \in \mathcal{N}(i)} w_u^i \hat{\mathbf{d}}_u}{\sum_{u \in \mathcal{N}(i)} w_u^i}, \text{ with } w_u^i = \frac{1}{\|\mathbf{p}_i - \hat{\mathbf{p}}_u\|_2}, \quad (22)$$

where $\mathcal{N}(i)$ indicates the k -nearest neighbor ($k = 3$ in practice) of \mathbf{p}_i w.r.t. points $\hat{\mathbf{p}}_u$ s.t. $(\hat{\mathbf{p}}_u, \hat{\mathbf{q}}_v) \in \mathcal{C}$. NFMR is finally computed by:

$$\mathcal{F}_N(\mathcal{C}^* | \mathcal{C}) = \frac{1}{|\mathcal{C}^*|} \sum_{(\mathbf{p}_i, \mathbf{q}_j) \in \mathcal{C}^*} \mathbb{1}(\|\mathbf{d}_i - \mathbf{d}_i^*\|_2 < \tau_4), \quad (23)$$

with \mathbf{d}_i^* the ground-truth deformation flow and $\tau_4 = 0.04\text{m}$ in practice.

A.6. More Quantitative Results

Varying Correspondence Number on Rotated Data. We further analyze the performance of different methods w.r.t. the varying number of correspondences on rotated data. The superiority of RoITr can be observed in Tab. 7.

# Samples	Rotated 3DMatch					Rotated 3DLoMatch				
	5000	2500	1000	500	250	5000	2500	1000	500	250
<i>Feature Matching Recall (%)</i> ↑										
SpinNet [1]	97.4	97.4	96.7	96.5	94.1	75.2	74.9	72.6	69.2	61.8
Predator [19]	96.2	96.2	96.6	96.0	96.0	73.7	74.2	75.0	74.8	73.5
CoFiNet [50]	97.4	97.4	97.2	97.2	97.3	78.6	78.8	79.2	78.9	79.2
YOHO [44]	97.8	97.8	97.4	97.6	96.4	77.8	77.8	76.3	73.9	67.3
RIGA [49]	98.2	98.2	98.2	98.0	98.1	84.5	84.6	84.5	84.2	84.4
GeoTrans [29]	97.8	97.9	98.1	97.7	97.3	<u>85.8</u>	<u>85.7</u>	<u>86.5</u>	<u>86.6</u>	<u>86.1</u>
RoITr (Ours)	98.2	98.1	98.1	98.1	98.1	89.4	89.2	89.1	89.1	89.0
<i>Inlier Ratio (%)</i> ↑										
SpinNet [1]	48.7	46.0	40.6	35.1	29.0	25.7	23.9	20.8	17.9	15.6
Predator [19]	52.8	53.4	52.5	50.0	45.6	22.4	23.5	23.0	23.2	21.6
CoFiNet [50]	46.8	48.2	49.0	49.3	49.3	21.5	22.8	23.6	23.8	23.8
YOHO [44]	64.1	60.4	53.5	46.3	36.9	23.2	23.2	19.2	15.7	12.1
RIGA [49]	<u>68.5</u>	<u>69.8</u>	<u>70.7</u>	<u>71.0</u>	<u>71.2</u>	32.1	33.5	34.3	34.7	35.0
GeoTrans [29]	68.2	<u>72.5</u>	<u>73.3</u>	<u>79.5</u>	<u>82.3</u>	<u>40.0</u>	<u>40.3</u>	<u>42.7</u>	<u>49.5</u>	<u>54.1</u>
RoITr (Ours)	82.3	82.3	82.6	82.6	82.6	53.2	54.9	55.1	55.2	55.3
<i>Registration Recall (%)</i> ↑										
SpinNet [1]	93.2	93.2	91.1	87.4	77.0	61.8	59.1	53.1	44.1	30.7
Predator [19]	92.0	92.8	92.0	92.2	89.5	58.6	59.5	60.4	58.6	55.8
CoFiNet [50]	92.0	91.4	91.0	90.3	89.6	62.5	60.9	60.9	59.9	56.5
YOHO [44]	92.5	92.3	92.4	90.2	87.4	66.8	67.1	64.5	58.2	44.8
RIGA [49]	<u>93.0</u>	<u>93.0</u>	<u>92.6</u>	<u>91.8</u>	<u>92.3</u>	66.9	67.6	67.0	66.5	66.2
GeoTrans [29]	92.0	91.9	91.8	91.5	91.4	<u>71.8</u>	<u>72.0</u>	<u>72.0</u>	<u>71.6</u>	<u>70.9</u>
RoITr (Ours)	94.7	94.9	94.4	94.4	94.2	77.2	76.5	76.6	76.5	76.0

Table 7. Quantitative results on Rotated 3DMatch & 3DLoMatch with a varying number of points/correspondences.

Ablation Study on (Rotated) 3DMatch. We also conduct ablation study on (Rotated) 3DMatch, as shown in Tab. 8. Similar to the ablation study on (Rotated) 3DLoMatch shown in the main paper, our default model achieves

the best performance, which further confirms the significance of each individual design of RoITr.

Category	Model	3DMatch					
		Origin			Rotated		
		FMR	IR	RR	FMR	IR	RR
a. Local	1. PT [54]	96.7	71.0	87.6	96.4	69.5	90.5
	*2. PPF+PT [54]	97.9	80.1	91.2	97.8	79.8	93.9
	3. Δ_{xyz} +Ours	-	-	-	-	-	-
	*4. Ours	98.0	82.6	91.9	98.2	82.3	94.7
b. Aggregation	*1. max pooling	97.9	80.8	90.7	97.8	80.8	94.1
	*2. avg pooling	98.1	81.8	92.1	98.2	81.8	94.8
	*3. Ours	98.0	82.6	91.9	98.2	82.3	94.7
c. Backbone	1. KPConv [40]	97.9	74.6	91.1	97.3	72.8	94.3
	*2. Ours	98.0	82.6	91.9	98.2	82.3	94.7
d. Global	*1. GeoTrans [29]	97.9	82.6	90.8	98.0	82.3	94.5
	*2. Ours	98.0	82.6	91.9	98.2	82.3	94.7
e. #Global	*1. $g = 0$	98.5	65.8	90.9	98.3	65.9	93.7
	*2. $g = 1$	98.4	74.8	90.8	98.5	74.8	94.2
	*3. $g = 3$ (Ours)	98.0	82.6	91.9	98.2	82.3	94.7
	*4. $g = 5$	98.1	82.0	91.7	98.0	82.0	94.6

Table 8. Ablation study on (Rotated) 3DMatch. 5,000 points/correspondences are leveraged. * indicates the methods with intrinsic rotation invariance.

A.7. More Qualitative Results

Indoor Scenes: 3DLoMatch. We show more qualitative results on the challenging 3DLoMatch benchmark in Fig. 9. **Deformable Objects: 4DLoMatch.** More qualitative results of the 4DLoMatch benchmark consisting of partially-scanned deformable objects are demonstrated in Fig. 10.

A.8. Runtime

We show the runtime comparison with Leopard [21] and GeoTrans [29] in Tab. 9. We run all the methods on a machine with a single Nvidia RTX 3090 GPU and an AMD Ryzen 5800X 3.80GHz CPU. All the models are tested without CPU parallel and with a batch size of 1. All the reported time is averaged over the 3DMatch testing set that consists of 1,623 point cloud pairs. The column "Data" counts the runtime for data preparation, and the column "Model" reports the time for generating descriptors from the prepared data. As shown in Tab. 9, RoITr has the highest data preparation and overall speed while the lowest model speed. That is mainly due to the relatively low speed of the attention mechanism compared to convolutions, e.g., KPConv [40] used in both Leopard and GeoTrans, and also because we do the Farthest Point Sampling (FPS) and k -nearest neighbor search on GPU, which is counted into the

Method	Data (s) ↓	Model (s) ↓	Total (s) ↓
Leopard [21]	0.444	0.051	0.495
GeoTrans [29]	<u>0.194</u>	<u>0.076</u>	<u>0.270</u>
RoITr (Ours)	0.023	0.210	0.233

Table 9. Runtime comparison.

model time.

A.9. Limitations

Further Discussion. Although RoITr achieves remarkable performance on both the rigid and non-rigid scenarios, we also notice the drawbacks of our method. The first is the efficiency of the attention mechanism. Although our local attention mechanism runs faster compared to that of Point Transformer [54], its running speed is still lower than that of convolutions, as shown in Tab. 9. Moreover, the intrinsic rotation invariance comes at the cost of losing the ability to match symmetric structures (see the 4DLoMatch data of Fig. 11). Furthermore, RoITr mainly relies on feature distinctiveness to implicitly filter out the occluded areas during the matching procedure, which makes it fail in cases with extremely limited overlap (see the 3DLoMatch data of Fig. 11). Finally, as normal data augmentation cannot work on intrinsically rotation-invariant methods, more data is required to train a larger model.

Failure Cases. We further show some failure cases in Fig. 11. It can be observed that the failure on 3DLoMatch is caused by an extremely limited overlap on the flattened areas. In the first row, the overlap ratio is only 17.6%, and the overlap region is mainly on the floor. In the second row, the overlap region is even more limited (with an overlap ratio of 10.7%) and mainly on a wall. For the 4DLoMatch, the failure is mainly due to the extremely limited overlap and the ambiguity caused by the symmetric structure. The first row shows a case with the two frames of point cloud showing a horse’s left and right parts, with only 18.1% overlap in the middle. The second row with 17.9% overlap ratio also has a strong left-right ambiguity due to the symmetric structure of a pig, which accounts for many left-right mismatches.

References

- [1] Sheng Ao, Qingyong Hu, Bo Yang, Andrew Markham, and Yulan Guo. Spinnet: Learning a general surface descriptor for 3d point cloud registration. In *CVPR*, 2021. 1, 2, 6, 7, 12
- [2] Jimmy Lei Ba, Jamie Ryan Kiros, and Geoffrey E Hinton. Layer normalization. *arXiv preprint arXiv:1607.06450*, 2016. 4, 11
- [3] Xuyang Bai, Zixin Luo, Lei Zhou, Hongbo Fu, Long Quan, and Chiew-Lan Tai. D3feat: Joint learning of dense detection and description of 3d local features. In *CVPR*, 2020. 2
- [4] Axel Barroso-Laguna, Yannick Verdie, Benjamin Busam, and Krystian Mikolajczyk. Hdd-net: Hybrid detector descriptor with mutual interactive learning. In *Proceedings of the Asian Conference on Computer Vision*, 2020. 2
- [5] Tolga Birdal and Slobodan Ilic. Point pair features based object detection and pose estimation revisited. In *3DV*, 2015. 4, 9
- [6] Christopher Choy, JunYoung Gwak, and Silvio Savarese. 4d spatio-temporal convnets: Minkowski convolutional neural networks. In *CVPR*, 2019. 1
- [7] Christopher Choy, Jaesik Park, and Vladlen Koltun. Fully convolutional geometric features. In *ICCV*, 2019. 1, 2
- [8] Chin Seng Chua and Ray Jarvis. Point signatures: A new representation for 3d object recognition. *IJCV*, 1997. 2
- [9] Haowen Deng, Tolga Birdal, and Slobodan Ilic. Ppf-foldnet: Unsupervised learning of rotation invariant 3d local descriptors. In *ECCV*, 2018. 1, 2, 4
- [10] Haowen Deng, Tolga Birdal, and Slobodan Ilic. Ppfnet: Global context aware local features for robust 3d point matching. In *CVPR*, 2018. 1, 2, 9
- [11] Bertram Drost, Markus Ulrich, Nassir Navab, and Slobodan Ilic. Model globally, match locally: Efficient and robust 3d object recognition. In *CVPR*, 2010. 1, 2
- [12] Martin A Fischler and Robert C Bolles. Random sample consensus: a paradigm for model fitting with applications to image analysis and automated cartography. *Communications of the ACM*, 1981. 6
- [13] Zan Gojcic, Caifa Zhou, Jan D Wegner, and Andreas Wieser. The perfect match: 3d point cloud matching with smoothed densities. In *CVPR*, 2019. 1, 2
- [14] Yulan Guo, Ferdous Sohel, Mohammed Bennamoun, Min Lu, and Jianwei Wan. Rotational projection statistics for 3d local surface description and object recognition. *IJCV*, 2013. 2
- [15] Ji Hou, Benjamin Graham, Matthias Nießner, and Saining Xie. Exploring data-efficient 3d scene understanding with contrastive scene contexts. In *CVPR*, 2021. 1
- [16] Ji Hou, Saining Xie, Benjamin Graham, Angela Dai, and Matthias Nießner. Pri3d: Can 3d priors help 2d representation learning? In *ICCV*, 2021. 1
- [17] Chun-Hao Huang, Benjamin Allain, Jean-Sébastien Franco, Nassir Navab, Slobodan Ilic, and Edmond Boyer. Volumetric 3d tracking by detection. In *CVPR*, 2016. 1
- [18] Chun-Hao Paul Huang, Benjamin Allain, Edmond Boyer, Jean-Sébastien Franco, Federico Tombari, Nassir Navab, and Slobodan Ilic. Tracking-by-detection of 3d human shapes: from surfaces to volumes. *TPAMI*, 2017. 1
- [19] Shengyu Huang, Zan Gojcic, Mikhail Usvyatsov, Andreas Wieser, and Konrad Schindler. Predator: Registration of 3d point clouds with low overlap. In *CVPR*, 2021. 1, 2, 5, 6, 7, 8, 9, 11, 12
- [20] Diederik P Kingma and Jimmy Ba. Adam: A method for stochastic optimization. *arXiv preprint arXiv:1412.6980*, 2014. 9
- [21] Yang Li and Tatsuya Harada. Leopard: Learning partial point cloud matching in rigid and deformable scenes. In *CVPR*, 2022. 1, 2, 6, 7, 8, 9, 12, 15
- [22] Yang Li, Hikari Takehara, Takafumi Taketomi, Bo Zheng, and Matthias Nießner. 4dcomplete: Non-rigid motion estimation beyond the observable surface. In *ICCV*, 2021. 7
- [23] Richard A Newcombe, Dieter Fox, and Steven M Seitz. Dynamicfusion: Reconstruction and tracking of non-rigid scenes in real-time. In *CVPR*, 2015. 1

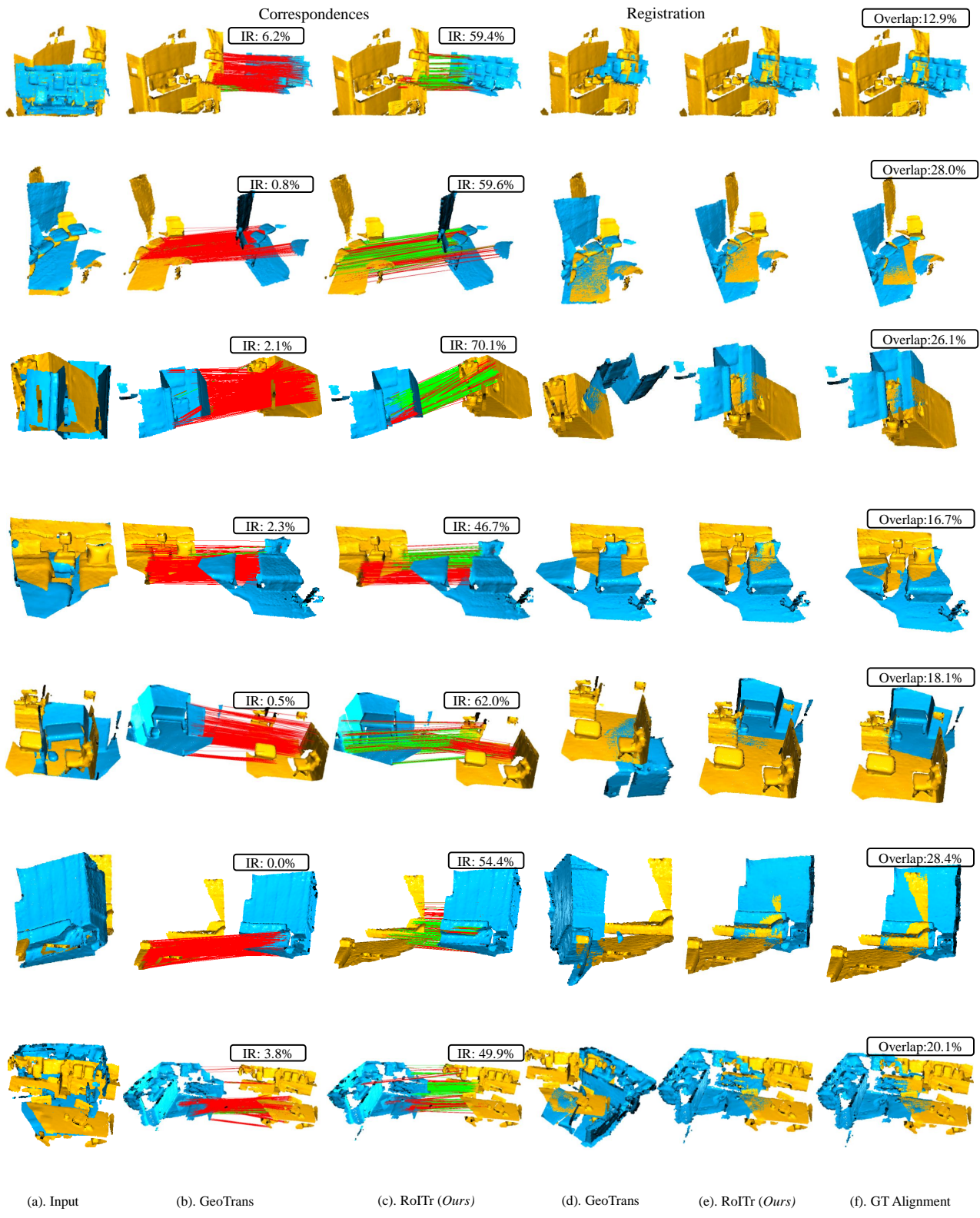


Figure 9. More qualitative results on 3DLoMatch. GeoTrans [29] is used as the baseline.

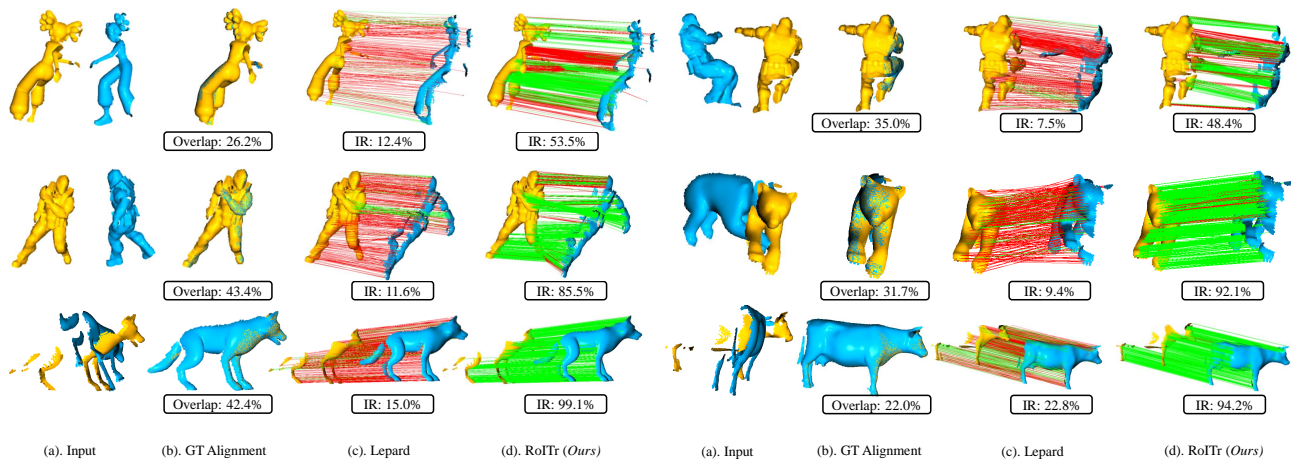


Figure 10. More qualitative results on 4DLoMatch. Leopard [21] is used as the baseline.

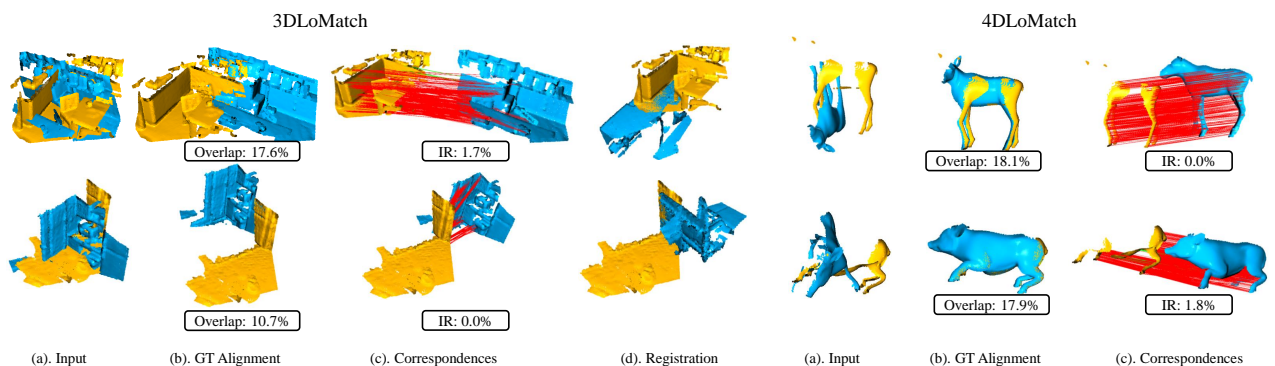


Figure 11. Failed cases on 3DLoMatch and 4DLoMatch.

- [24] Richard A Newcombe, Shahram Izadi, Otmar Hilliges, David Molyneux, David Kim, Andrew J Davison, Pushmeet Kohi, Jamie Shotton, Steve Hodges, and Andrew Fitzgibbon. Kinectfusion: Real-time dense surface mapping and tracking. In *IEEE International Symposium on Mixed and Augmented Reality*, 2011. 1
- [25] Adam Paszke, Sam Gross, Francisco Massa, Adam Lerer, James Bradbury, Gregory Chanan, Trevor Killeen, Zeming Lin, Natalia Gimelshein, Luca Antiga, et al. Pytorch: An imperative style, high-performance deep learning library. *NeurIPS*, 2019. 9
- [26] Gilles Puy, Alexandre Boulch, and Renaud Marlet. Flot: Scene flow on point clouds guided by optimal transport. In *ECCV*, 2020. 7
- [27] Charles R Qi, Hao Su, Kaichun Mo, and Leonidas J Guibas. Pointnet: Deep learning on point sets for 3d classification and segmentation. In *CVPR*, 2017. 1, 2, 8
- [28] Charles Ruizhongtai Qi, Li Yi, Hao Su, and Leonidas J Guibas. Pointnet++: Deep hierarchical feature learning on point sets in a metric space. *NeurIPS*, 2017. 1, 3, 4, 8
- [29] Zheng Qin, Hao Yu, Changjian Wang, Yulan Guo, Yuxing Peng, and Kai Xu. Geometric transformer for fast and robust point cloud registration. In *CVPR*, 2022. 1, 2, 5, 6, 7, 8, 9, 12, 14
- [30] Ignacio Rocco, Mircea Cimpoi, Relja Arandjelović, Akihiko Torii, Tomas Pajdla, and Josef Sivic. Neighbourhood consensus networks. *NeurIPS*, 2018. 5
- [31] Radu Bogdan Rusu, Nico Blodow, and Michael Beetz. Fast point feature histograms (fpfh) for 3d registration. In *ICRA*, 2009. 1, 2
- [32] Radu Bogdan Rusu, Nico Blodow, Zoltan Csaba Marton, and Michael Beetz. Aligning point cloud views using persistent feature histograms. In *IROS*, 2008. 1, 2
- [33] Mahdi Saleh, Shervin Dehghani, Benjamin Busam, Nassir Navab, and Federico Tombari. Graphite: Graph-induced feature extraction for point cloud registration. In *3DV*, 2020. 1, 2
- [34] Mahdi Saleh, Yige Wang, Nassir Navab, Benjamin Busam, and Federico Tombari. Cloudattention: Efficient multi-scale attention scheme for 3d point cloud learning. *arXiv preprint arXiv:2208.00524*, 2022. 1
- [35] Mahdi Saleh, Shun-Cheng Wu, Luca Cosmo, Nassir Navab, Benjamin Busam, and Federico Tombari. Bending graphs:

- Hierarchical shape matching using gated optimal transport. In *CVPR*, 2022. 1, 2
- [36] Paul-Edouard Sarlin, Daniel DeTone, Tomasz Malisiewicz, and Andrew Rabinovich. Superglue: Learning feature matching with graph neural networks. In *CVPR*, 2020. 6, 11
- [37] Richard Sinkhorn and Paul Knopp. Concerning nonnegative matrices and doubly stochastic matrices. *Pacific Journal of Mathematics*, 1967. 6
- [38] Jiaming Sun, Zehong Shen, Yuang Wang, Hujun Bao, and Xiaowei Zhou. Loftr: Detector-free local feature matching with transformers. In *CVPR*, 2021. 5
- [39] Yifan Sun, Changmao Cheng, Yuhan Zhang, Chi Zhang, Liang Zheng, Zhongdao Wang, and Yichen Wei. Circle loss: A unified perspective of pair similarity optimization. In *CVPR*, 2020. 9
- [40] Hugues Thomas, Charles R Qi, Jean-Emmanuel Deschaud, Beatriz Marcotegui, François Goulette, and Leonidas J Guibas. Kpconv: Flexible and deformable convolution for point clouds. In *ICCV*, 2019. 1, 8, 12
- [41] Federico Tombari, Samuele Salti, and Luigi Di Stefano. Unique signatures of histograms for local surface description. In *ECCV*, 2010. 1, 2
- [42] Giovanni Trappolini, Luca Cosmo, Luca Moschella, Riccardo Marin, Simone Melzi, and Emanuele Rodolà. Shape registration in the time of transformers. *NeurIPS*, 2021. 2
- [43] Ashish Vaswani, Noam Shazeer, Niki Parmar, Jakob Uszkoreit, Llion Jones, Aidan N Gomez, Łukasz Kaiser, and Illia Polosukhin. Attention is all you need. *NeurIPS*, 2017. 5, 7, 9
- [44] Haiping Wang, Yuan Liu, Zhen Dong, and Wenping Wang. You only hypothesize once: Point cloud registration with rotation-equivariant descriptors. In *ACM MM*, 2022. 2, 6, 7, 12
- [45] Wenxuan Wu, Zhiyuan Wang, Zhuwen Li, Wei Liu, and Li Fuxin. Pointpwc-net: A coarse-to-fine network for supervised and self-supervised scene flow estimation on 3d point clouds. *arXiv preprint arXiv:1911.12408*, 2019. 7
- [46] Saining Xie, Jiatao Gu, Demi Guo, Charles R Qi, Leonidas Guibas, and Or Litany. Pointcontrast: Unsupervised pre-training for 3d point cloud understanding. In *Computer Vision—ECCV 2020: 16th European Conference, Glasgow, UK, August 23–28, 2020, Proceedings, Part III 16*, pages 574–591. Springer, 2020. 1
- [47] Yaoqing Yang, Chen Feng, Yiru Shen, and Dong Tian. Foldingnet: Point cloud auto-encoder via deep grid deformation. In *CVPR*, 2018. 2
- [48] Zi Jian Yew and Gim Hee Lee. Regtr: End-to-end point cloud correspondences with transformers. In *CVPR*, 2022. 1, 2, 5
- [49] Hao Yu, Ji Hou, Zheng Qin, Mahdi Saleh, Ivan Shugurov, Kai Wang, Benjamin Busam, and Slobodan Ilic. Riga: Rotation-invariant and globally-aware descriptors for point cloud registration. *arXiv preprint arXiv:2209.13252*, 2022. 1, 2, 5, 6, 7, 11, 12
- [50] Hao Yu, Fu Li, Mahdi Saleh, Benjamin Busam, and Slobodan Ilic. Cofinet: Reliable coarse-to-fine correspondences for robust pointcloud registration. *NeurIPS*, 2021. 1, 2, 3, 5, 6, 7, 8, 10, 12
- [51] Wentao Yuan, Benjamin Eckart, Kihwan Kim, Varun Jampani, Dieter Fox, and Jan Kautz. Deepgmr: Learning latent gaussian mixture models for registration. In *ECCV*, 2020. 11
- [52] Andy Zeng, Shuran Song, Matthias Nießner, Matthew Fisher, Jianxiong Xiao, and Thomas Funkhouser. 3dmatch: Learning local geometric descriptors from rgb-d reconstructions. In *CVPR*, 2017. 1, 2, 6, 9
- [53] Yu Zhang, Junle Yu, Xiaolin Huang, Wenhui Zhou, and Ji Hou. Pcr-cg: Point cloud registration via deep explicit color and geometry. In *ECCV*, 2022. 1
- [54] Hengshuang Zhao, Li Jiang, Jiaya Jia, Philip HS Torr, and Vladlen Koltun. Point transformer. In *ICCV*, 2021. 1, 2, 7, 8, 12, 13